MULTISCALE MECHANICAL CHARACTERIZATION OF FIBRIN GELS

by

Julian Jimenez

A Thesis

Submitted to the Faculty of Purdue University

In Partial Fulfillment of the Requirements for the degree of

Master of Science in Biomedical Engineering

Weldon School of Biomedical Engineering

West Lafayette, Indiana

August 2021

THE PURDUE UNIVERSITY GRADUATE SCHOOL
STATEMENT OF COMMITTEE APPROVAL

Dr. Sarah Calve, Chair
Weldon School of Biomedical Engineering

Dr. Adrian Buganza-Tepole
School of Mechanical Engineering

Dr. Luis Solorio
Weldon School of Biomedical Engineering

Approved by:
Dr. George R. Wodicka

ACKNOWLEDGMENTS

This work is supported by the NSF CMMI 1911346. I would like to thank Dr. Sarah Calve, Dr. Adrian Buganza-Tepole, and Dr. Luis Solorio for their guidance and mentorship throughout my development as a graduate student, and for giving me the opportunity to be a part of a creative and collaborative research environment. I would also like to thank all members of the Musculoskeletal Extracellular Matrix Lab (MEML) for their support throughout my time at Purdue University and at the University of Colorado, Boulder. Particularly, I would like to thank Andrea Acuña and Yue Leng for their guidance and collaborative efforts on this project, Callan Luetkemeyer for the development of the slider device mentioned herein, Yifan Guo for the development of computational models mentioned herein, and Sean Rothenberger and Brandon Hayes for assistance with 3D printing.

TABLE OF CONTENTS

LIST OF FIGURES

LIST OF ABBREVIATIONS

AF – Alexa Fluor

AFM – Atomic Force Microscopy

DFN – Discrete Fiber Network

ECM – Extracellular Matrix

FE – Finite Element

FOV – Field of View

PBS – Phosphate Buffered Saline

PE – Porous Polyethylene

PET – Polyethylene terephthalate

RT – Room Temperature (20 – 22°C)

ROI – Region of Interest

RVE – Representative Volume Element

SEM – Scanning Electron Micrography

SD – Standard Deviation

ABSTRACT

The extracellular matrix (ECM) is a dynamic network of biomolecules that provides tissues with structural organization and regulates cellular behavior. Cells remodel the ECM at the micro- (1-10 μm) and mesoscales (10-1000 μm) in response to mechanical and biochemical stimuli, ultimately changing the macroscale (1-10 mm) mechanical properties of tissues. Thus, understanding the relationships between the macroscale tissue mechanics and the mesoscale ECM structure is needed across biomedical applications, for example, in the design of scaffolds that provide a transient matrix to support and promote wound healing and regeneration after injury. Common scaffolding materials include biopolymers like collagen and fibrin.

Fibrin is a naturally occurring protein that forms a temporary structure for remodeling during wound healing. It is also a common tissue engineering scaffold because its structural properties can be controlled. Here, we present a strategy to quantify the multiscale mechanics of fibrin gels by measuring both the macroscale stress-strain response and the deformation of the mesoscale fibrin network structure during uniaxial tensile tests. This information can be used to inform multiscale computational models that predict how alterations of the microstructural properties of the ECM influence macroscale mechanical properties and, reciprocally, how macroscale deformations lead to changes in the structure and organization of the cellular microenvironment.

While homogeneous scaffolds are commonly used to support tissue constructs, these do not accurately recapitulate the organization of the ECM *in vivo*, particularly, near interfacial tissue boundaries where ECM composition, organization, and density can differ drastically (*e.g.* tumor and the surrounding stroma, wound surrounded by healthy tissue). To address this gap, we developed an *in vitro* model using heterogeneous fibrin gels to recapitulate an interfacial ECM boundary. We first informed a computational model with the experimentally-determined stress-strain response and organization of homogeneous fibrin gels. The model was then used to predict the non-uniform stress and strain of a heterogeneous fibrin gel under uniaxial tension. The simulations were compared with experimentally measured macroscale stress and strain of heterogeneous fibrin gels, confirming the predictive capabilities of the computational model. The strategies proposed here can be extended to characterize the multiscale mechanics of other biological materials and improve scaffold design, including complex interfacial ECM boundaries between tissues.

1. INTRODUCTION

1.1 Extracellular Matrix and Biomedical Scaffolding

The extracellular matrix (ECM) is a dynamic network of biomolecules that provides structural organization and regulates cellular behavior. Mechanical and biochemical signaling transmitted by the ECM to the cells can elicit acute cell responses such as cell migration, proliferation, differentiation, and protein secretion. The ECM also regulates cellular behavior during dynamic events over longer time scales such as in growth, healing, regeneration, and development (Urbanczyk et al., 2020). Here, we focus on mechanotransudction, which is a critical factor in the regulation of cellular activity. For example, substrate stiffness influences cellular differentiation. Seeding human mesenchymal stem cells in soft (0.6 kPa) polyacrylamide gels leads to differentiation into adipocytes, whereas seeding the same cells in stiff (70 kPa) polyacrylamide gels leads to differentiation into osteocytes (Frith et al., 2018). In addition to stiffness, deformations and stresses developed in the ECM can also regulate cellular activity. For example, human dermal, pulmonary, and cardiac fibroblast cells show increased type I collagen and fibronectin deposition when cultured on a substrate that is stretched compared to a static substrate (Breen, 2000; Kessler et al., 2001; Lindahl et al., 2002). Thus, mechanical forces and deformations at the macroscale, on the order of 1-10mm, are transmitted to the resident cells through the ECM, and lead to remodeling of the micro- and mesoscale environment on the order of 1 – 10 μm to 10 – 1000 μm, respectively (Brown et al., 2009; Gilchrist et al., 2014; Lloyd et al., 2015). Structural changes to the ECM at the mesoscale ultimately alter the macroscale mechanical properties of tissues (Brown et al., 2009; Gilchrist et al., 2014; Lloyd et al., 2015).

Tissue engineering applications hinge on developing scaffolds that mimic properties of the ECM at the micro- and mesoscales to promote desired cellular responses as well as macroscale mechanical function, for instance in wound healing and regeneration. While scaffolds that are homogeneous in composition and organization (*e.g.* single concentration collagen or fibrin gels) are commonly used to support tissue constructs, these do not entirely recapitulate the variable characteristics of the ECM that are observed *in vivo* (Moutos & Guilak, 2008), particularly, tissues near interfacial boundaries where ECM composition, organization, and density can differ drastically (Bordeleau et al., 2013; Tonti et al., 2021). One example of ECM heterogeneity is the

temporary fibrin clot within a wound, which is less stiff than the surrounding tissue which is typically composed of more stiff, crosslinked Type I and Type III collagen networks (Miron-Mendoza et al., 2017; Schultz et al., 2005).

In addition to developing scaffolds with biomedical applications such as wound healing and regeneration, scaffolds are also developed to study the development of disease pathologies, *e.g.* the progression of cancer tumors. Fibrin gels, in particular heterogeneous fibrin gels, can be used to better understand the mechanobiology of complex biological systems in physiologically relevant *in vitro* models. For instance, the ECM proximal to a solid cancer tumor tends to be much more dense and stiff compared to ECM more distal to the tumor (Bordeleau et al., 2013).

Scaffolds that combine various materials have been engineered to achieve mechanical and biological properties that more closely resemble the tumor and wound microenvironments (Bordeleau et al., 2013; Miron-Mendoza et al., 2017; Moutos & Guilak, 2008). However, these scaffolds do not entirely recapitulate temporospatial mechanical cues necessary to guide cellular behavior towards wound healing and regeneration (Nikolova & Chavali, 2019). Further studies into the non-uniform stress-strain of these scaffolds and how they influence cellular behavior are needed. Characterizing the non-uniform mechanics of these scaffolds is critical to understanding how variations in material properties influence cellular behavior. Optimizing design parameters will result in the development of scaffolding materials that provide the appropriate mechanical cues to guide healing and regeneration.

1.2 Fibrin Structure and Formation

Fibrin is a naturally occurring protein that is polymerized from fibrinogen monomers following vascular injury and provides a temporary structure to stop bleeding and for remodeling during wound healing (Janmey et al., 2009). It is a common tissue engineering scaffold because fibrin can be cast into gels that are biocompatible and its structural properties (*e.g.* fiber length, diameter, fibrin volume fraction) can be controlled by modulating fibrinogen and thrombin concentrations (Janmey et al., 2009).

Fibrinogen monomers are composed of two symmetric halves, each composed of an Aα, Bβ, and γ peptide chains (Fig. 1.1). The amino termini of the six chains come together to form a central nodule. The carboxy terminal ends of the Bβ and γ chains form the end nodules, β-nodule and γ.

The carboxy terminal of the Aα chain is termed the αC region (Ryan et al., 1999; Weisel & Litvinov, 2013; Zhmurov et al., 2016).

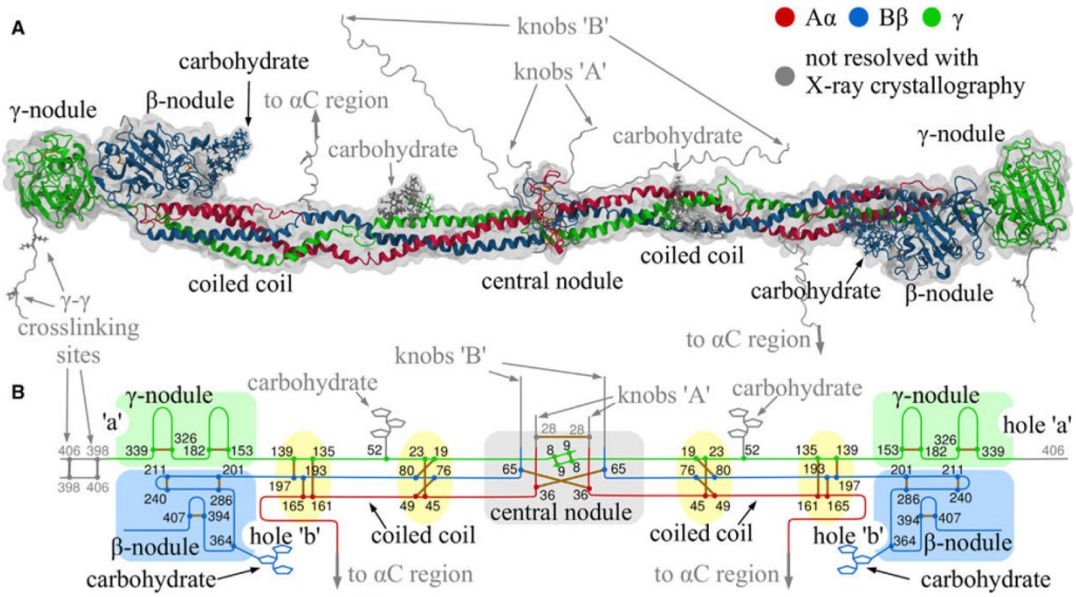

Figure 1.1. **Fibrinogen monomer structure** (Zhmurov et al., 2016)

Fibrinogen is typically found circulating blood plasma at concentrations of 1.5 – 3.5 mg/mL (Fish & Neerman-Arbez, 2012; Weisel & Litvinov, 2017). Under blood flow conditions, fibrinogen is added to the growing fibrin clot (Neeves et al., 2010; Weisel & Litvinov, 2017), increasing the overall fibrin content by two-fold per hour (Silvain et al., 2011). The presence of fibrinopeptides A and B at the ends of the Aα and Bβ amino terminal ends on the central nodule of the fibrinogen monomer prevent the spontaneous aggregation of fibrinogen monomers. Vascular injury initiates a biochemical cascade that triggers the conversion of prothrombin, which circulates in the blood at concentrations of 1 – 2 μM (Ryan et al., 1999), to the proteolytic enzyme thrombin. The fibrin polymerization reaction is initiated when thrombin cleaves fibrinopeptides A and B from the fibrinogen monomers, exposing “knob” A and “knob” B. These “knobs” are free to bind to complementary sites, “hole” a and “hole” b, which are located on the γ-nodule and β-nodule, respectively (Fig. 1.2) (Weisel & Litvinov, 2013). In this way, fibrin monomers bind longitudinally in a half-staggered configuration, forming fibrin oligomers. Fibrin oligomers continue to elongate longitudinally to produce protofibrils, which are typically composed of 20-25 fibrin monomers (Weisel & Litvinov, 2017). Protofibrils then begin to aggregate laterally through various weak and strong binding interactions, to form fibrin fibers. One mode of lateral

aggregation is the binding of αC chains to form αC- αC polymers between protofibrils (Brown et al., 2007; Weisel & Litvinov, 2013). Binding of calcium ions to has Ca^{2+} binding cites on fibrin γ chains has been shown to enhance protofibril lateral aggregation (Weisel & Litvinov, 2017). Ca^{2+} is typically found in blood plasma at concentrations of 1.5 – 2 mM (Ryan et al., 1999). As fibrin fibers continue to elongate and aggregate laterally, branching points from leading to the 3D network structure of fibrin gels. The abundance and rate of fibrin aggregation creates a balance between elongation and lateral aggregation. Branching typically occurs as part of the fiber elongation process. Therefore, enhanced lateral aggregation will lead to thicker fibers and fewer branch points, while lower lateral aggregation will lead to thinner fibers and more branch points (Weisel & Litvinov, 2017). Factor XIIIa covalently crosslinks α-γ and γ-γ chains between protofibrils within a fibrin fiber to create a more mechanically and chemically stable 3D network (Ryan et al., 1999; Weisel & Litvinov, 2013).

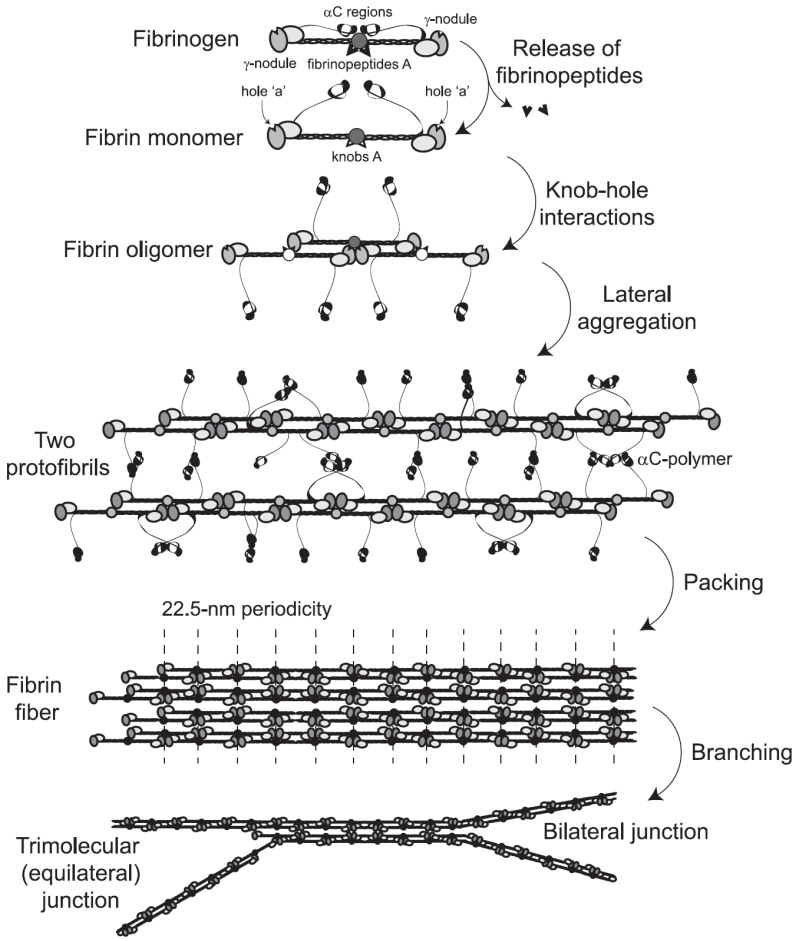

Figure 1.2. **Fibrin formation and hierarchy** (Weisel & Litvinov, 2013)

At the molecular scale, transmission electron micrography (Brown et al., 2007), X-ray crystallography, and atomic force microscopy have been used to visualize structure and composition of fibrin monomers and oligomers (Weisel & Litvinov, 2017; Zhmurov et al., 2016).

The mesoscale organization of fibrin networks has been visualized with namely with scanning electron microscopy (SEM) (Ryan et al., 1999) and confocal microscopy (Britton et al., 2019; Wang et al., 2021). SEM imaging can be performed on fixed and dehydrated fibrin gels at magnifications between 4,000x and 25,000x (Ryan et al., 1999). Confocal imaging of fluorescently conjugated fibrin can be performed on hydrated fibrin samples at magnifications ranging between 10x and 100x (Britton et al., 2019; Magatti et al., 2013; Wang et al., 2021). Characteristics of interest at the mesoscale that have been measured include fiber length, fiber diameter, branching density (*i.e.* number of fibers at a single branch point), branch point density (*i.e*. number of branch points within a given volume), fiber density, fiber orientation, and pore size (Ryan et al., 1999; Weisel & Litvinov, 2017). Approaches to quantifying these parameters in fibrin gels and other hydrogels or network structures have included ImageJ plugins (Wang et al., 2021), commercially available software packages like IMARIS (Podhorská et al., 2020), Amira (Xia et al., 2021), and custom image processing algorithms (Lai et al., 2012; Molteni et al., 2013).

The formation of fibrin gels is influenced by external factors like protein and enzyme concentrations, ionic strength, and pH (Weisel & Litvinov, 2017). The structure and material properties of fibrin gels *in vitro* can be modulated by altering the concentrations of fibrinogen, thrombin, and Ca^{2+} that modulate polymerization kinetics. For example, increasing the fibrinogen concentration minimally affects fiber length and diameter, but can notably influence fibril density and branch-point density (Fig. 1.3 A). Increasing the thrombin concentration can decrease fiber length and fiber diameter, and increase fiber density and branch-point density (Fig. 1.3B). Increasing the calcium ion concentration can increase fiber length and diameter, and decrease fiber density and branch-point density (Fig. 1.3 C) (Ryan et al., 1999). Modulating parameters that influence fibrin structure resulted in fiber length averages ranging from 0.3 ± 0.2 μm to 4.8 ± 3.5 μm with a total range of 0.1 – 19 μm. Average fiber diameters ranged from 44 ± 15 nm to 147 ± 59 nm with a total range of 16 – 391 nm (Ryan et al., 1999).

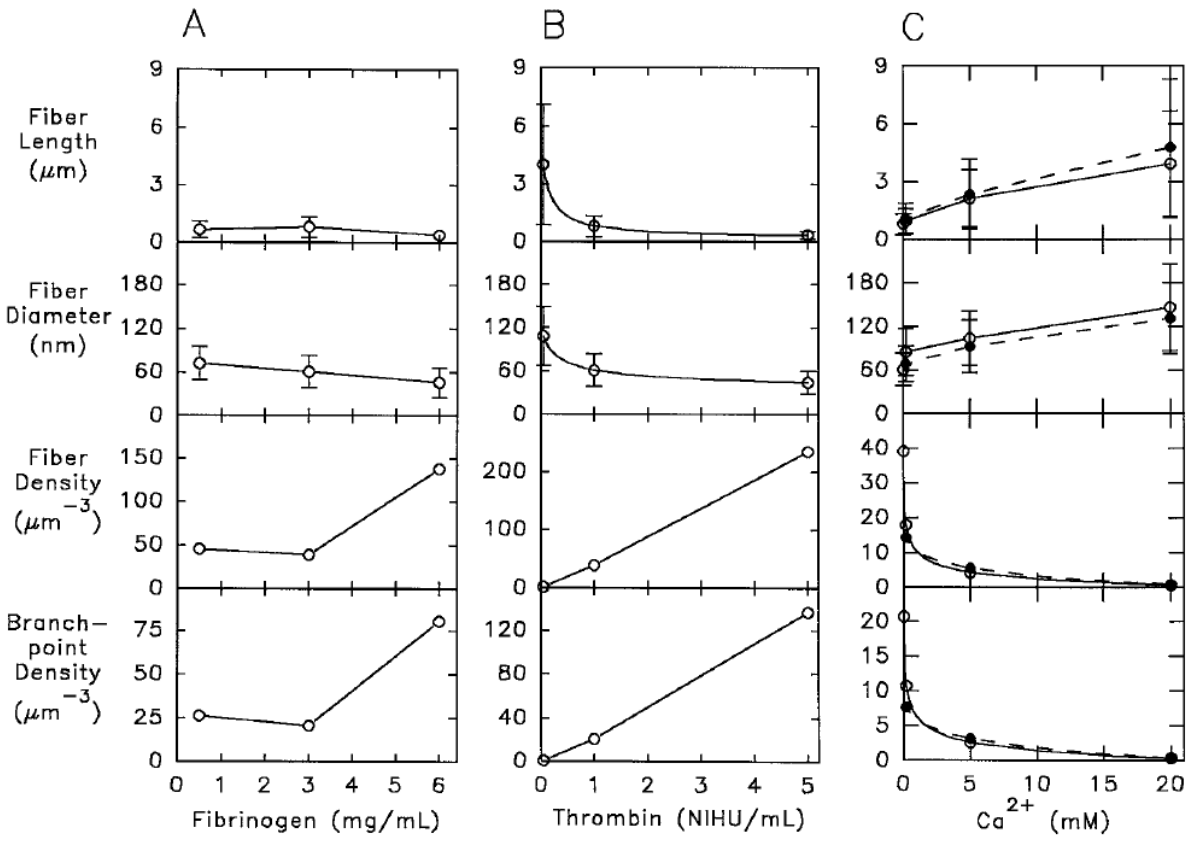

Figure 1.3. **Modulating fibrin gel structure**. (Ryan et al., 1999)

1.3 Fibrin Gel Mechanics

The mechanics of fibrin have been studied at various hierarchical scales, namely, the macroscale, mesoscale, and molecular level mechanics. As a bulk material, fibrin is a viscoelastic polymer (Weisel, 2004). The viscous and elastic properties of fibrin gels have been studied with rheology and tensile testing. In this study, we focus on the effects of tension on the mechanical properties of fibrin because of an interest in the tensile forces exerted onto fibrin clots during wound healing (Tepole, 2017). Additionally, since fibrin gels are arranged in a fibrillar structure, they contribute to the mechanics of tissues in tension.

Under tension, fibrin gels have a linear stress-strain response at strains below $\varepsilon \approx 1.2$. For strains greater than $\varepsilon \approx 1.2$ fibrin gels have a non-linear stress-strain response, with an increase in the equilibrium tangent modulus for a given strain (Brown et al., 2009; Janmey et al., 2009). At the molecular scale, atomic force microscopy has been used to evaluate the extensibility of fibrin

monomers and oligomers under tension while measuring force. This data has been complemented by transmission electron micrography images of the molecules under tension (Brown et al., 2007; Li et al., 2017; Yesudasan & Averett, 2020).

At the mesoscale, fibrin gels' network distribution in static conditions tends to be isotropic. While this microstructure is often also representative of in vivo conditions, *e.g.* in wound clots, fibrin *in vivo* can also form anisotropic gels. Fibrin formed under flow conditions, *e.g.* blood flow, result in fibrin fibers orientation in the direction of flow (Campbell et al., 2010; Weisel & Litvinov, 2017). Therefore, anisotropic fibrin gels generated under flow in vitro have also been developed (Campbell et al., 2010). Here we only focus on isotropic gels. Under uniaxial tension, the network of fibrin fibers gradually aligns in the direction of tension (Fig. 1.4) (Brown et al., 2009).

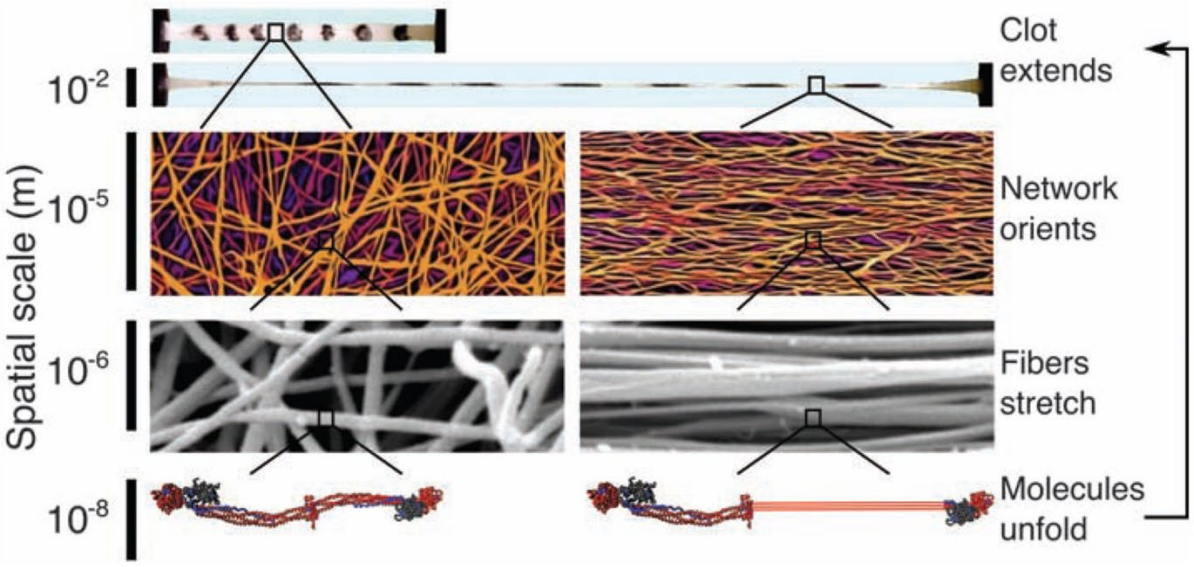

Figure 1.4. **Structural hierarchy of fibrin governs mechanical properties**. Left $\varepsilon = 0$, Right $\varepsilon \approx 2$ (Brown et al., 2009)

As strain increases, gradually, individual fibrin fibers begin to stretch. As fibers stretch, their diameter decreases and fibers bundle closer together, expelling water, increasing the fiber density, and decreasing the overall volume of the gel (Brown et al., 2009). As the macroscale deformation increases, uniaxial tension of fibers extends down to protofibrils and individual fibrin monomers. Molecular unfolding of coiled Aα, Bβ, γ peptide chains, as well as αC-αC connections leads to the high extensibility and non-linear strain hardening of the hierarchical fibrin structure at large strains (Brown et al., 2009; Weisel & Litvinov, 2017). General trends at the macroscale that come from

the mesoscale include greater gel stiffness with increasing fiber density, branch point density, and fiber diameter (Ryan et al., 1999).

Imaging modalities have been used to visualize the mesoscale structural changes of fibrin gels under dynamic conditions, *e.g.* during fibrin formation and fibrinolysis (Collet et al., 2000), and under shear stress and tensile stress (Britton et al., 2019; Münster et al., 2013; Wang et al., 2021). However, visualizing the fibrin gel mesoscale structure during deformation while simultaneously coupling tensile stress and strain information has not been achieved. A challenge in evaluating tensile test mechanics and visualizing mesoscale deformation, is that the modalities to perform uniaxial tension of soft biomaterials while simultaneously visualizing sample deformation, and keeping the sample hydrated are largely undeveloped. Here we present a system that can be used to characterize macroscale mechanics of fibrin gels, and adapt it so that it can also be used to simultaneously visualize the mesoscale deformation of the gels during tensile testing and stress relaxation. The details regarding the development and verification of the system are shown in APPENDIX A.

1.4 Informing Multiscale Predictive Models

Multiscale models can be used to describe and predict how macroscale deformation influences the microscale structures that are relevant to cellular mechanobiology. Conversely, multiscale models can also predictively describe how structural changes at the micro- and mesoscale during ECM remodeling events like wound healing, regeneration, and development, influence the functional mechanical properties of the ECM and their respective tissues, at the macroscale. Once these models are developed, they can be used to run simulations predicting how altering the structural parameters of fibrin gels would influence the macroscale mechanical properties. This computational approach would speed up the development of scaffolding with desired structural and mechanical properties by optimizing design parameters through iterative simulations, rather than through experimental approaches. Once parameters and boundary conditions are defined, experimentally challenging tests like biaxial or triaxial testing can be simulated and stress-strain fields can be estimated (Ban et al., 2019). Computational models are also advantageous when it comes to describing non-uniform mechanics that would be challenging to characterize empirically, like those of heterogeneous materials. Additionally, computational

methods like inverse finite element (FE) models can be used to derive material properties when experimental testing is not possible (Buganza Tepole et al., 2014).

Characterizing micro- and mesoscale structural properties of fibrin gels under tensile deformation, alongside the macroscale stress and strain, can be used to inform multiscale computational models. Various models have been proposed to model the multiscale mechanical behavior of three-dimensional hydrogel networks. For example, a discrete fiber networks (DFN) models individual fibers with defined parameters for fiber length, fiber diameter, distribution of fiber orientation, and volume fraction of fibers all within a representative volume element (RVE) of the fiber network mesh (Abhilash et al., 2014; Ban et al., 2019; Leng et al., 2021). The structural deformation of the DFN can be used to guide FE simulations to derive the macroscale mechanical behavior of the bulk material (Leng et al., 2021).

Structural and mechanical measurements of homogeneous fibrin gels at the mesoscale and macroscale can inform FE models of non-uniform, heterogeneous gels. This strategy can be adapted to predict and characterize the stress-strain distribution of novel engineered scaffolds that are variable in both geometry complexity and material composition to better recapitulate the heterogeneous composition of the ECM.

2. MATERIALS AND METHODS

2.1 Fibrin Gel Polymerization

Fibrin gels were polymerized using 3D-printed molds and laser-cut frames to control fibrin gel geometry and facilitate uniaxial tensile testing. Porous polyethylene (PE) blocks were used as anchor points for fibrin gel constructs (Fig. 2.1).

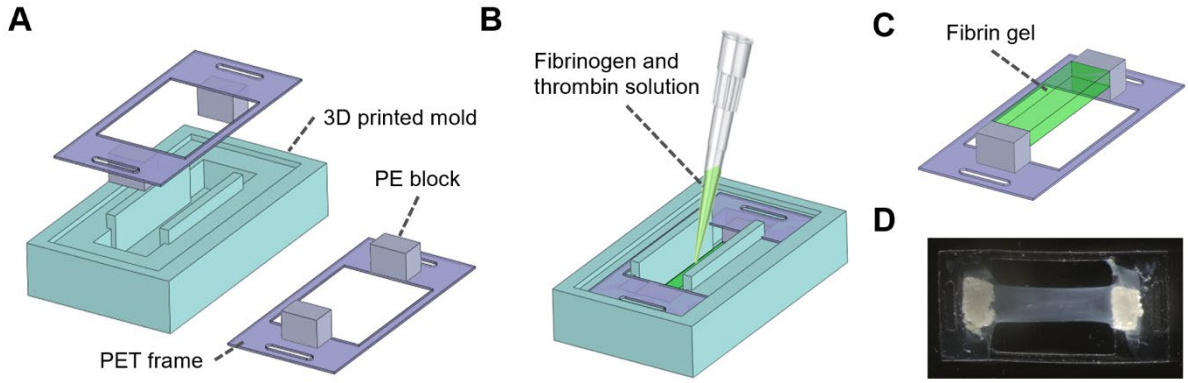

Figure 2.1. **Fibrin gel preparation.** (A) PET frames with PE blocks spaced 6.6 mm apart were inverted and placed within 3D-printed molds. (B) Fibrinogen and thrombin solutions were pipetted into the mold and allowed to settle for approximately 5 minutes. (C) Fibrin gel constructs were then removed from the mold and placed in PBS. (D) Fibrin gel construct with 2 mg/mL fibrinogen concentration.

Molds were designed on SolidWorks (Dassault Systèmes) and 3D printed (Stratasys J750) with a photopolymer (VeroClear, Stratasys) with properties similar to acrylic. Frames with 6 mm x 12 mm (w x l) were drawn in Adobe Illustrator (AI) and laser cut from 100 µm thick polyethylene terephthalate (PET) using the Speedy 400 (Trotec). PE blocks (Coarse Grade, Bel-Art Products) were manually cut to approximately 1.5 mm x 2.0 mm x 1.5 mm (w x l x h). PE blocks were incubated in 70% ethanol for 5 minutes at room temperature (RT) to wet the internal surface area of the PE, to increase hydrophilicity and, thus, increase permeability to solubilized fibrinogen. Ethanol-soaked PE blocks were then incubated in a 12.91 mg/mL fibrinogen solution (FIB3, Enzyme Research Laboratories) for at least 1 hour. Fibrinogen-soaked PE blocks were bonded onto frames using UV curable resin (Thin-Hard Formula, Solarez) and then irradiated with UV light for 60 seconds to cure the resin. Frames were then inverted and placed within the molds.

Homogeneous fibrin concentrations of 2, 4, and 6 mg/mL were prepared in 2.5 mm x 6.6 mm x 0.75 mm (w x l x h) molds by combining human fibrinogen (12.91 mg/mL; FIB3, Enzyme Research Laboratories) and Alexa Fluor (AF) 488 conjugated human fibrinogen (1 mg/mL; F-13191, Molecular Probes) at a 1:10 fluorescent to non-fluorescent fibrinogen ratio, 2M $CaCl_2$, and 0.5 U thrombin (HT 1002A, Enzyme Research Laboratories) per mg fibrinogen in phosphate buffered saline (PBS). Heterogeneous fibrin constructs were made by first pipetting 2 mg/mL AF 488-labeled fibrin into a 4 mm x 6.6 mm x 0.75 mm mold, as described above, and then pipetting 4 mg/mL AF 546-labeled fibrin into the center of the 2 mg/mL fibrin as it polymerized. Fibrinogen and thrombin solutions were pipetted into the mold and allowed to settle for approximately 5 minutes. Forceps were then used to carefully remove the frame from the molds. Frames with fibrin constructs were immediately placed in room temperature PBS to keep samples hydrated.

Molds were designed with five positions to allow the polymerization of multiple fibrin constructs simultaneously. The molds were reused and cleaned in between use to remove any fibrin gel that adhered to surfaces during polymerization. Molds were placed in a 70% EtOH solution for 5 minutes, 0.1% Triton solution for at least 60 minutes, and MilliQ water solution for at least 60 minutes all on a rocker at room temperature.

2.2 Macroscale Tensile Testing

Fiducial lines were photobleached onto fibrin in a vertical pattern or a 5 x 5 grid pattern using a Leica STELLARIS 5 confocal microscope and a 10x Apochromatic dry (NA = 0.40) objective. A FemtoTools micromanipulator system (FT-RS1002), microforce sensor probe (FT-S100’000), custom 3D printed spring, and a Leica microscope camera (Infinity 3-URC) were used to collect force data and acquire video of sample deformation during uniaxial tensile testing as previously described (Duan et al., 2021; Enríquez et al., 2021) (APPENDIX A) (Fig. 2.2).

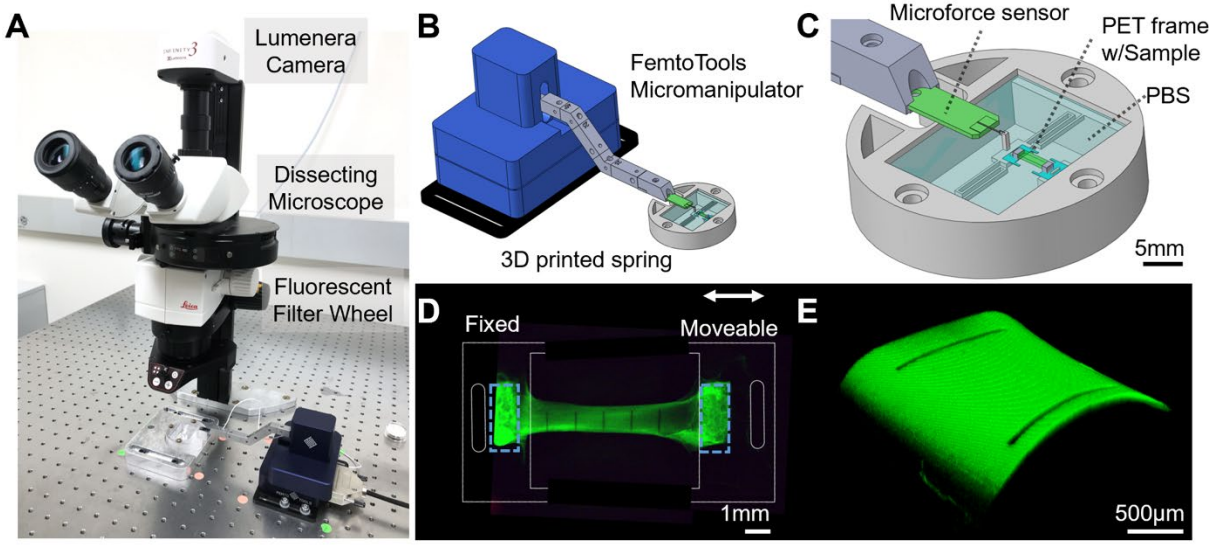

Figure 2.2. **Macroscale tensile testing system.** (A) Dissecting microscope and Lumenera camera assembly. (B) FemtoTools micromanipulator and spring assembly. (C) FemtoTools microforce sensor attached to 3D printer spring. PET frame with fibrin gel sample loaded on spring. (D) Fluorescently conjugated fibrin sample with fiducial lines on PET frame. PE blocks outlined in blue. (E) 3D rendering of fibrin.

Tensile tests were conducted at $0.01s^{-1}$ strain rate up to a 6000 µm displacement, equivalent to linear strain of $\varepsilon = 0.91$ based on micromanipulator displacement. Gels composed of 2 mg/mL (n = 4), 4 mg/mL (n = 4), and 6 mg/mL (n = 2) fibrinogen concentration were tensile tested.

2.3 Stress and Strain Data Analysis

For homogeneous fibrin, strain was calculated from the vertical fiducial lines through video analysis using a custom FIJI macro and MATLAB algorithm, as previously described (Enríquez et al., 2021). Linear strain was calculated by $(l_i - l_0)/l_0$, where l_0 is the initial distance between two fiducial lines, and l_i are subsequent distances. FIJI was used to measure the cross-sectional area of gels from acquired z-stacks. Nominal stress was calculated by dividing force data by the initial regional cross-sectional area, measured prior to mechanical testing. The tangent modulus was calculated from the stress-strain response of 2 mg/mL, 4 mg/mL, and 6 mg/mL fibrin gel samples.

For heterogeneous fibrin gel, FIJI was used to analyze videos and manually track the position of each vertex on the fiducial 5 x 5 grid (Fig. 3.5C). A custom Python code was used to plot the position of the vertices and calculate the Green Lagrange strain of each region.

2.4 Mesoscale Tensile Testing

The FemtoTools system was mounted on a custom platform atop the moving stage of the STELLARIS 5 confocal microscope and coupled with either a spring or slider (DA-6-NMS, Deltron) interface to mechanically characterize fibrin gel samples (Figure 2.3). The moving stage moved the entire FemtoTools system and fibrin sample in tandem relative to the fixed position of the confocal microscope objectives to facilitate imaging.

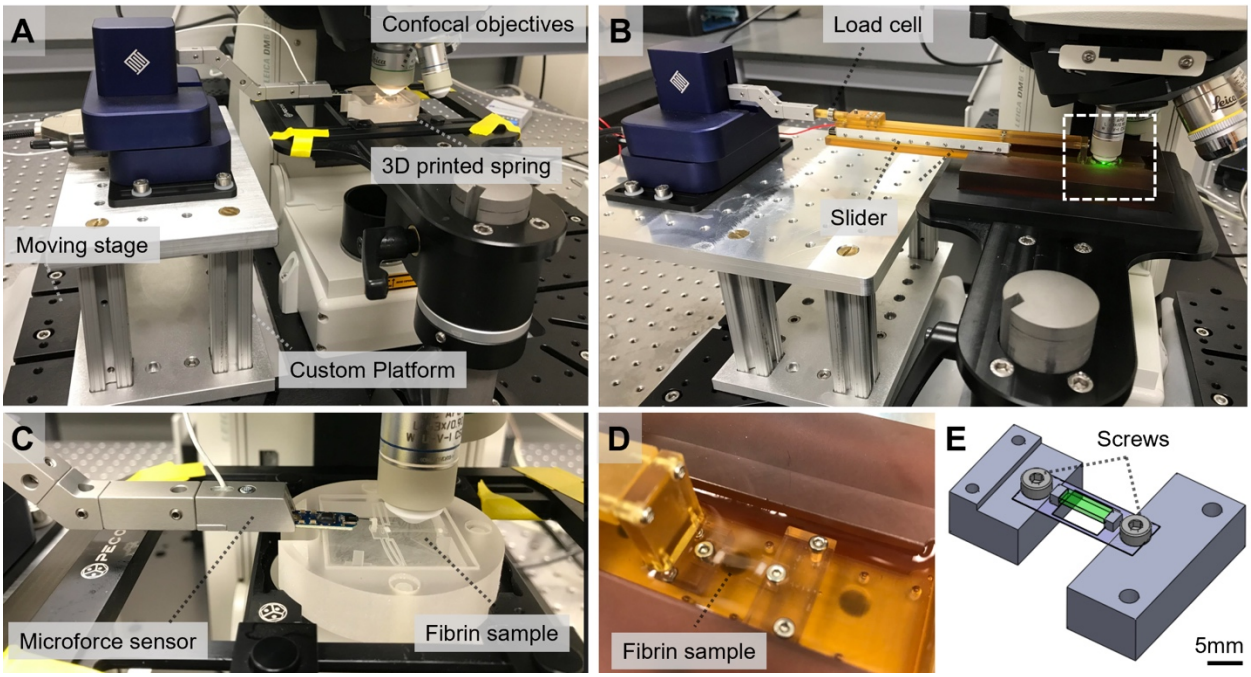

Figure 2.3. **Mesoscale tensile testing systems.** FemtoTools micromanipulator mounted on the moving platform of the Stellaris 5 confocal microscope coupled with a microforce sensor and 3D printed spring (A) and with a slider assembly (B). Fibrin samples were loaded onto the spring (C) or the slider assembly (D, E).

The FemtoTools and spring assembly (Fig. 2.3 A) was coupled with the FemtoTools microforce sensor (Fig. 2.3 C) to facilitate force acquisition throughout uniaxial tensile testing and confocal imaging. Minute fluid undulations within the PBS retention well caused the floating spring and fibrin sample to slightly undulate during confocal imaging. These minute movements diminished image resolution through the introduction of motion artifacts. While high resolution images could be collected with a 25x objective, the slight motion artifacts diminished the resolution of images acquired with a 63x objective. In order to supplement stress-strain and structural data gathered with the FemtoTools and spring system, a different configuration that

provided greater motion stability during imaging was utilized (see Figure 2.3B). The FemtoTools and slider assembly was used to image samples under tension using a 63x objective with minimal motion artifacts. The slider assembly was coupled with a Futek load cell (LCM100-1000g), however, the force contribution of the slider was notably higher than the contribution from the fibrin gel, and was not used to resolve the force contribution of fibrin samples. Screws were used to mount the PET frames loaded with fibrin samples to minimize movement.

Fiducial lines were photobleached onto the fibrin gels using either the 25x or 63x immersible objectives to track sample deformation throughout tensile testing. Tensile tests were conducted in increments of 1000 μm displacement at $0.01s^{-1}$ strain rate followed by a period of stress relaxation to allow the samples to reach a stable configuration and to accommodate confocal imaging in between displacement intervals. Fibrin gel samples were allowed to settle for at least 10 minutes after a displacement interval prior to imaging.

2.5 Mesoscale Structure Image Acquisition

Z-stacks were acquired to visualize the mesoscale fibrin structure during different loading conditions using a Leica STELLARIS 5 confocal microscope using a Fluotar 25x (NA = 0.95) and an Apochromatic 63x (NA = 0.90) water immersible objectives.

Static samples that did not undergo tensile testing were imaged directly on the 3D-printed mold in which the fibrin gels were polymerized. Z-stacks of representative volume elements (RVE) from the fibrin gel were acquired. Three samples of each fibrin gel concentration, 2 mg/mL, 4 mg/mL, and 6 mg/mL, were imaged. Three regions from each sample were imaged using the 63x objective at digital zooms 2.7, 6, and 12, with respective XY field of views (FOV) 63.4 μm x 63.4 μm, 29.4 μm x 29.4 μm, and 14.9 μm x 14.9 μm.

Samples that were uniaxially loaded on the FemtoTools and spring system underwent 10 minutes of stress-relaxation after each displacement interval prior to imaging. After the sample stabilized, z-stacks were acquired with a 25x objective, at digital zoom 6, with respective XY FOV of 70.3 μm x 70.3 μm, from a region equidistant from the two fiducial markers. After z-stack acquisition, the fiducial lines were measured with a tile scan using the 25x objective at a digital zoom of 0.75 with respective XY FOV of 590.5 μm x 590.5 μm.

Samples uniaxially loaded on the FemtoTools and slider system underwent 10 minutes of stress-relaxation after each displacement interval prior to imaging. Z-stacks were acquired with a

63x objective, at digital zoom of 2.7, 6, and 12 from a region equidistant from the two fiducial markers. After z-stack acquisition, the fiducial lines were measured with a tile scan using the 63x objective at a digital zoom of 0.75 with respective XY FOV of 234.3 μm x 234.3 μm.

Images were acquired and deconvoluted using the Leica LIGHTNING settings optimized for high resolution. Images acquired with the 25x objective had 0.0722 μm x 0.0722 μm XY resolution and 0.505 μm Z resolution with 0.5 NA pinhole diameter. Images acquired with a 63x objective had 0.0253 μm x 0.0253 μm XY resolution and 0.281 μm Z resolution with 0.5 NA pinhole diameter. All images were taken with bi-directional settings.

2.6 Mesoscale Structure Image Analysis

Deconvoluted images were imported to FIJI (NIH) for characterization. Volume fraction was measured by first adjusting the image threshold to binarize pixels into fluorescence and background, then the BoneJ (Doube et al., 2010) Area/Volume Fraction function counted all fluorescent pixels and divided by the total number of pixels for each slice in the z-stack to estimate the fibrin volume fraction. Fiber diameters were manually measured on FIJI from maximum intensity projections of thin (0.5 – 1.5 μm) substacks. Fibers (n = 100) were measured for each z-stack. Fiber orientation distributions were measured using the FIJI OrientationJ algorithm. XY z-stacks were analyzed without pre-processing. XZ z-stacks were resliced from XY stacks at an interval matching the XY resolution (0.0253 μm for 63x, 0.0722 for 25x), grouped into approximately 0.5 μm thick maximum intensity z-projections using the Grouped Z Project function, and filtered with a Gaussian blur prior to analyzing. The structure tensors were computed using the 'Cubic Spline' gradient, and selecting a Local Window approximate to the average fiber diameter of each z-stack. The OrientationJ Analysis (Püspöki et al., 2016) function was used to visually evaluate the fit of the local window size for each z-stack that was analyzed. The OrientationJ Distribution (Rezakhaniha et al., 2012) function was then run using the Cubic Spline gradient, the optimized local window size, and a Minimum Coherency and Minimum Energy of 1%. The counts for each orientation (-90° to 90°, with 0.5° intervals) were summed across all of the slices of each stack, and then the counts for each orientation were normalized by the total sum for all orientations. The orientation distribution for the XY and XZ plane was taken orthogonal to the plane in the direction of uniaxial tension (x-axis), such that alignment with the direction of tension was 0 degrees. Fiber lengths were manually measured on FIJI from maximum intensity

XY projections of thin (0.5 – 1.5 μm) substacks from the OrientationJ Analysis output, to aid with fiber visualization. Fibers (n = 100) were measured for each z-stack. The length of a fiber was measured by tracing the path between two branch points.

One-way ANOVA with Tukey post hoc tests were performed to evaluate statistical differences among measurements for samples that varied in fibrinogen concentration and increasing tensile displacement.

2.7 Finite Element Analysis

An FE model was created in Abaqus to simulate the heterogeneous fibrin gel. The geometry of the FE model was based on measurements taken from confocal images of the heterogeneous fibrin gel. Clamped boundary conditions were imposed on the left side of the geometry, and the right side was stretched to 1.5x the original length, equivalent to $\varepsilon = 0.5$. We used a 2D FE model with plain stress assumptions and primarily 50 x 50 μm quadrilateral mesh elements with triangular elements to fill gaps where quadrilateral elements could not be used. The Gasser-Ogden-Holzapfel (GOH) (Gasser et al., 2006) was used in Abaqus to simulate the material, with parameters obtained by fitting the bulk material response for 2 mg/mL and 4 mg/mL fibrin. Stress-strain data from different locations on the heterogeneous fibrin, encompassing and adjacent to the 4 mg/mL fibrin inclusion, were isolated for comparison. To calculate the homogenized stress and strain response of the fibrin gel from the computational model, the stress of all mesh elements in the FE model were averaged for a given strain based on boundary deformation.

3. RESULTS

3.1 Macroscale Mechanical Characterization of Fibrin

Confocal imaging of homogeneous fibrin showed that fibril density increased with higher fibrinogen concentration (Fig. 3.1 C-E).

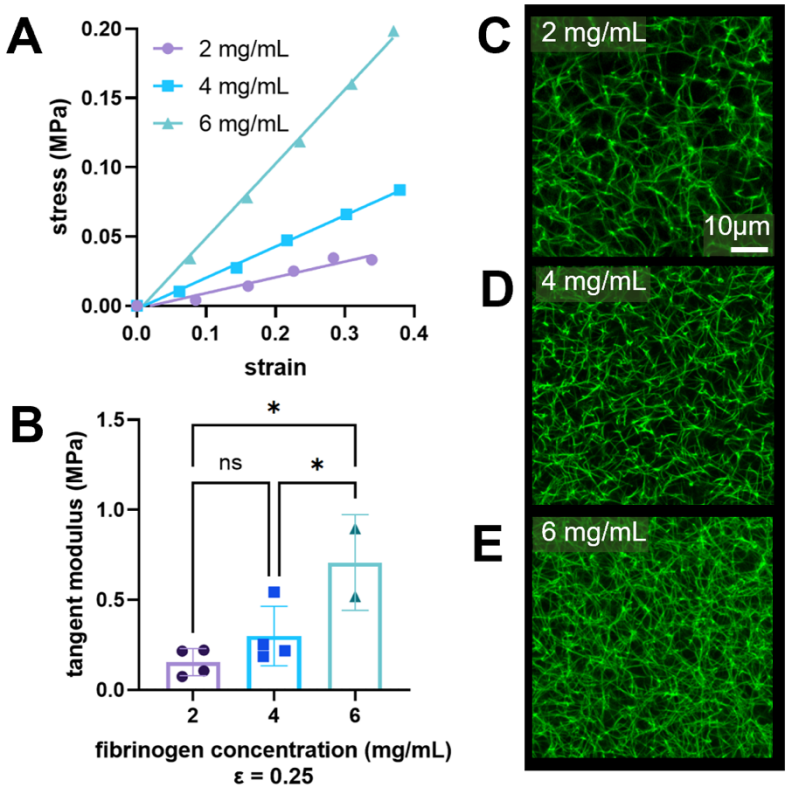

Figure 3.1. **Macroscale mechanical characterization of fibrin gels.** (A) Representative nominal stress v. linear strain curves for 2, 4, and 6 mg/mL fibrin. (B) Comparison of tangent moduli at ε = 0.25 (n = 2-4). Error bars = S.D. There was a statistically significant difference between concentrations as determined by the one-way ANOVA ($p < 0.05$), followed by Tukey multiple comparison post hoc test. ns $p > 0.05$; *$p < 0.05$. Mesoscale structure of 2 mg/mL (C), 4 mg/mL (D), and 6 mg/mL (E) fibrin.

A positive correlation between fibrinogen concentration and stiffness was observed. The average tangent moduli and standard deviation of the 2, 4, and 6 mg/mL fibrin at ε = 0.25 were 0.15 ± 0.08 MPa, 0.30 ± 0.16 MPa, and 0.71 ± 0.26 MPa, respectively (Fig. 3.1 B). There was a statistically significant difference between fibrinogen concentrations as determined by one-way

ANOVA ($p < 0.05$). There were statistically significant ($p < 0.05$) differences between the average tangent modulus of the 6 mg/mL fibrin gel and each of the 2 mg/mL and 4 mg/mL gels.

3.2 Mesoscale Mechanical Characterization

Static Configuration

The static configurations of 2 mg/mL, 4 mg/mL, and 6 mg/mL fibrin gels polymerized in a 3D-printed mold were imaged with a 63x objective and analyzed for structural differences. Z-stacks with $(29\ \mu m)^3$ (Fig. 3.2 A-F) and $(14\ \mu m)^3$ (Fig. 3.2 G-H) dimensions were acquired. The orientation of fibers from the perspective of the XY plane, and relative to the longitudinal geometry of the gel (x-axis), was similar across all concentrations (Fig. 3.2 I). There was no notable alignment in a particular orientation, indicating that the fibers were randomly aligned. In the XZ plane (Fig. 3.2 J), relative to the longitudinal geometry of the gel (x-axis), there appeared to be a relative peak in alignment at the ±90° orientation, suggesting that fibers were aligned vertically (z-axis). The average fibrin volume fraction and standard deviation for different regions (n=3) of each of the 2, 4, and 6 mg/mL fibrin gels was 0.06 ± 0.01, 0.13 ± 0.01, and 0.16 ± 0.03, respectively (Fig. 3.2 K), There was a statistically significant volume fraction difference between concentrations as determined by the one-way ANOVA ($p < 0.01$). There were statistically significant differences between the 2 mg/mL and 4 mg/mL ($p < 0.05$) and 2 mg/mL and 6 mg/mL ($p < 0.01$). The average and standard deviation for fiber diameters ($n = 100$) for 2, 4, and 6 mg/mL fibrin gels was 0.30 ± 0.10 µm, 0.26 ± 0.07 µm, and 0.27 ± 0.08 µm, respectively (Fig. 3.2 L) There was a statistically significant fiber diameter difference between concentrations from one-way ANOVA ($p < 0.0001$). There were significant differences between 2 mg/mL and 6 mg/mL ($p < 0.01$), and 2 mg/mL and 4 mg/mL ($p < 0.0001$). Fiber length was defined as the length of the path between two branch points observed in thin z-projections. The average and standard deviation for fiber lengths ($n = 100$) for 2, 4, and 6 mg/mL fibrin gels was 3.16 ± 1.35 µm, 2.81 ± 1.36 µm, and 2.44 ± 1.19 µm, respectively (Fig. 3.2 M). There was a statistically significant fiber length difference between concentrations from one-way ANOVA ($p < 0.01$), with statistically significant differences between 2 mg/mL and 6 mg/mL ($p < 0.001$).

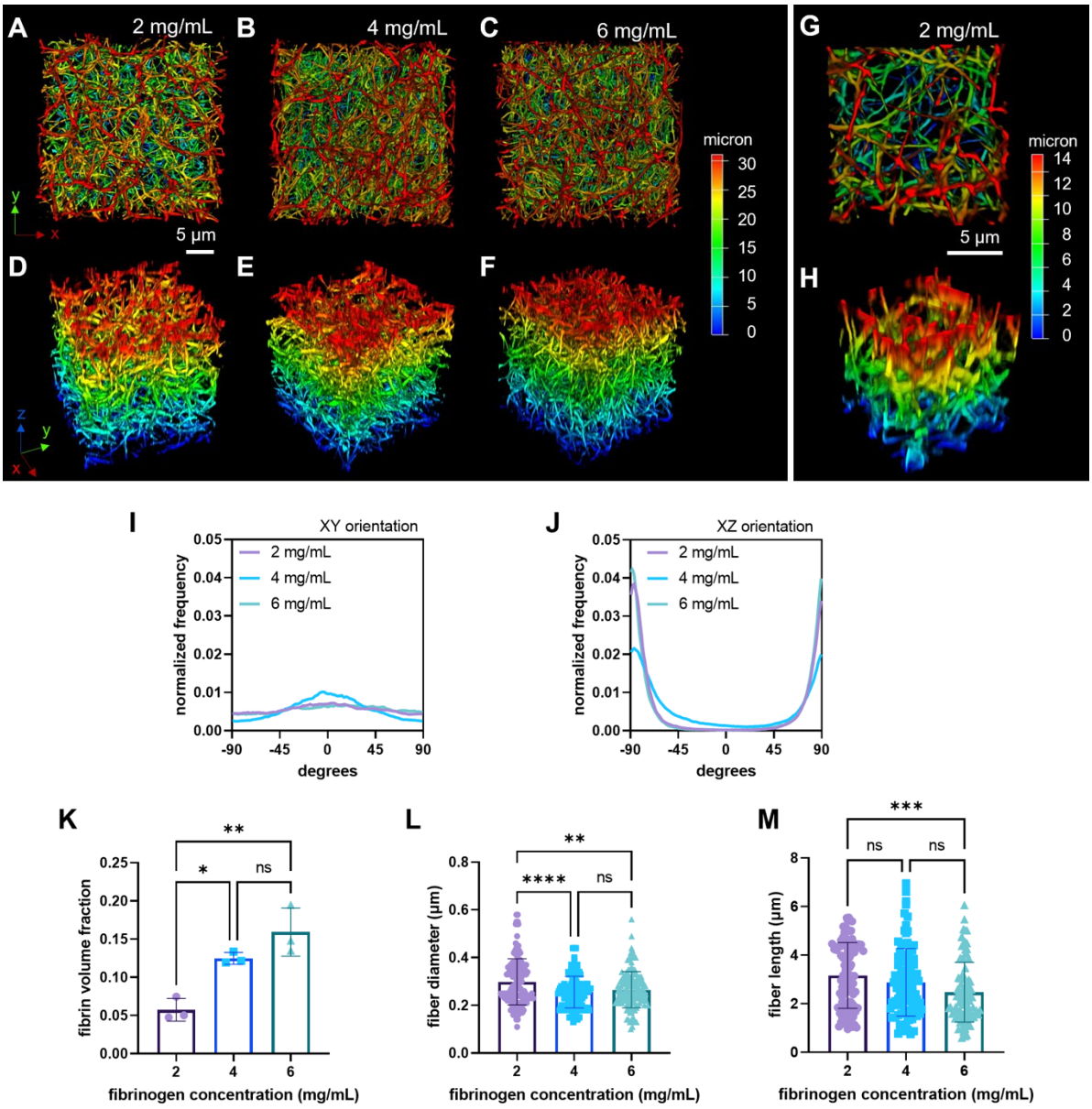

Figure 3.2. **Mesoscale characterization of fibrin gels within mold.** Three-dimensional rendering of 2, 4, and 6 mg/mL fibrin gels with a $(29\ \mu m)^3$ ROI. Top view, orthogonal to XY plane (A-C), and isometric view (D-F). Top (G) and isometric (H) views of representative 2 mg/mL fibrin gel rendering with a $(15\ \mu m)^3$ ROI. XY (I) and XZ (J) fiber orientation for 2, 4, and 6 mg/mL fibrin gels. (K) Average (±SD) fibrin volume fraction from z-stacks (n = 3) collected for each fibrinogen concentration. Statistically significant volume fraction difference between concentrations from one-way ANOVA ($p < 0.01$). (L) Average (±SD) fiber diameter (n = 100) collected for each fibrinogen concentration. Statistically significant fiber diameter difference between concentrations from one-way ANOVA ($p < 0.0001$) (M) Average (±SD) fiber length (n = 100) collected for each fibrinogen concentration. Statistically significant fiber length difference between concentrations from one-way ANOVA ($p < 0.01$). All statistical analyses are from a one-way ANOVA followed by Tukey's post hoc test, ns, $p > 0.05$, * $p < 0.05$, ** $p < 0.01$, *** $p < 0.001$, **** $p < 0.0001$.

Configuration Under Tension - Spring

Using the FemtoTools and spring system, a 2 mg/mL fibrin gel (n = 1) was imaged with a 25x objective and analyzed for structural differences, while simultaneously acquiring force and displacement information from tensile testing and stress relaxation. Z-stacks with (70 μm)^3 dimensions were acquired at displacements δ = 0, 1000, 2000, 3000, and 4000 μm (Fig. 3.3 A-J). Fiducial markers measured after z-stack imaging yielded strain values ε = 0, 0.10, 0.23, 0.35, and 0.56 for the respective displacements. The nominal stress-time curve displays incremental 1000 μm imposed deformations applied at a 0.01s^{-1} strain rate followed by 20 minutes of stress relaxation (Fig. 3.3 K). In the XY plane, and relative to the direction of uniaxial tension (x-axis), fiber alignment in the 0° orientation (x-axis) increased as a function of displacement (Fig. 3.3 L). Peak normalized frequencies for alignment in the 0° orientation for δ = 0, 1000, 2000, 3000, and 4000 μm were 0.005, 0.013, 0.024, 0.033, and 0.043, respectively. The magnification and resolution of z-stacks acquired on the spring system were not sufficient to resolve fibril alignment in the XZ plane.

There was an observed increase in fibrin volume fraction as the fibrin gel was uniaxially stretched (Fig. 3.3 M). The volume fraction (n = 1) was 0.10, 0.30, 0.30, 0.35, 0.34 for displacements δ = 0, 1000, 2000, 3000, and 4000 μm. There were no statistically significant differences between the diameters of the fibrin gel at different displacements as determined by the one-way ANOVA ($F(4,495) = 0.1231$, $p = 0.9742$). The average and standard deviation for fiber diameters (n = 100) for δ = 0, 1000, 2000, 3000, and 4000 μm was 0.38 ± 0.12 μm, 0.38 ± 0.13 μm, 0.38 ± 0.11 μm, 0.38 ± 0.10 μm, and 0.38 ± 0.11 μm, respectively (Fig. 3.3 N), The resolution of these images combined with increased fiber density, was not sufficient to confidently measure fiber as the gels were deformed. Measurement of fiber length was restricted to the unloaded configuration.

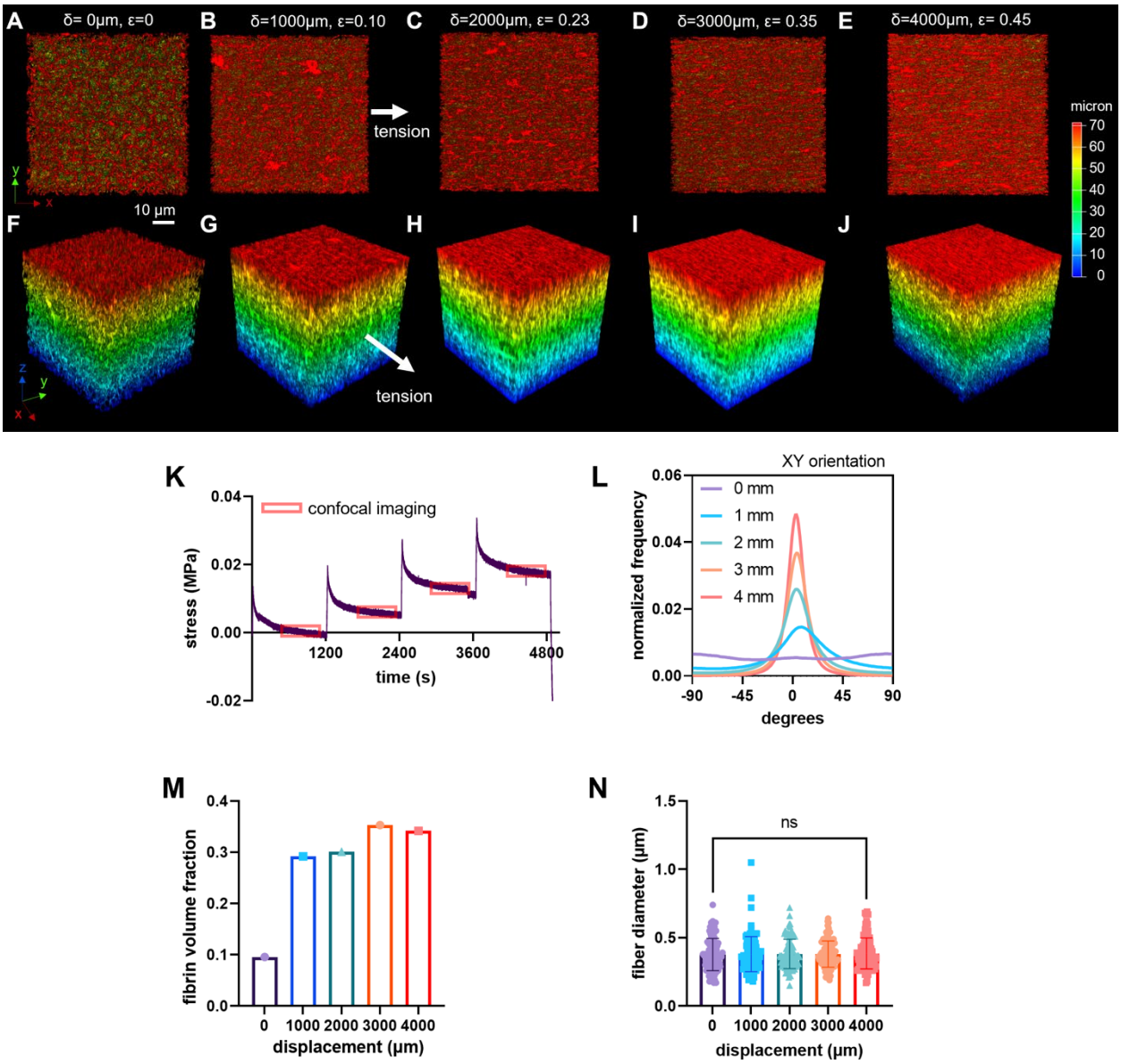

Figure 3.3. **Mesoscale characterization of 2 mg/mL fibrin gel network structure under uniaxial tension with the spring assembly**. Three dimensional renderings of fibrin gel displaced to δ = 0, 1000, 2000, 3000, and 4000 μm with a (74 μm)^3 ROI. Top view, orthogonal to the XY plane (A-E) and isometric views (F-J). (K) Uniaxial tensile tests (δ = 1000 μm intervals) followed by 20 minutes of stress relaxation to allow for material stabilization and image acquisition. Confocal image acquisition time window denoted by red rectangles. (L) XY fiber orientation for δ= 0-4000 μm displacements. (M) Fibrin volume fraction (n =1) for δ= 0-4000 μm displacements. (N) Average (±SD) fiber diameter (n=100) collected for each displacement. There were no statistically significant fiber diameter differences between displacements from the one-way ANOVA ($p > 0.05$) followed by Tukey's post hoc Test. ns, $p > 0.05$.

Configuration Under Tension – Slider

Using the FemtoTools and slider system, a of 2 mg/mL fibrin gel (n = 1) was imaged with a 63x objective and analyzed for structural differences, during tensile deformation. Z-stacks with $(29\ \mu m)^3$ dimensions were acquired at displacements δ = 1000, 2000, 3000, 4000, and 9000 μm (Fig. 3.4 A-J). Resolving individual fibers with the 63x objective at δ = 0 μm was not possible because when the sample was not held under tension, slight undulations introduced motion artifacts resulting in blurry imaging. Fiducial markers measured after z-stack imaging yielded strain values ε = 0.12, 0.25, 0.37, and 1.09 for the respective displacements. In the XY plane, and relative to the direction of uniaxial tension (x-axis), fiber alignment in the 0° orientation (x-axis) increased as a function of displacement (Fig. 3.4 K). Peak normalized frequencies for XY alignment in the 0° orientation for δ = 1000, 2000, 3000, 4000, and 9000 μm were 0.010, 0.021, 0.028, 0.041, and 0.083, respectively. In the XZ plane, and relative to the direction of uniaxial tension (x-axis), fiber alignment in the 0° orientation (x-axis) increased as a function of displacement (Fig. 3.4 L). Peak normalized frequencies for XZ alignment in the 0° orientation for δ = 1000, 2000, 3000, 4000 μm were 0.009, 0.013, 0.019, and 0.019, respectively. Resolution in the XZ plane combined with increased fiber density was not sufficient to accurately measure fiber alignment at δ = 9000 μm. There was an observed increase in fibrin volume fraction as the fibrin gel was uniaxially stretched (Fig. 3.4 M). The volume fraction (n = 1) was 0.10, 0.30, 0.30, 0.35, 0.34 for displacements δ = 0, 1000, 2000, 3000, and 4000 μm. The average and standard deviation for fiber diameters (n = 100) for δ = 1000, 2000, 3000, 4000, and 9000 μm was 0.29 ± 0.07 μm, 0.29 ± 0.08 μm, 0.26 ± 0.08 μm, 0.27 ± 0.08 μm, and 0.28 ± 0.06 μm, respectively (Fig. 3.4 N). There were statistically significant fiber diameter differences between displacements from the one-way ANOVA ($p < 0.0001$), with significant differences between δ = 1000 and δ = 3000 ($p < 0.01$), δ = 2000 and δ = 3000 ($p < 0.001$), δ = 2000 and δ = 4000 ($p < 0.05$), and δ = 3000 and δ = 9000 ($p < 0.05$). The resolution of these images was not sufficient to confidently measure fiber lengths past the 3000 μm displacement configuration.

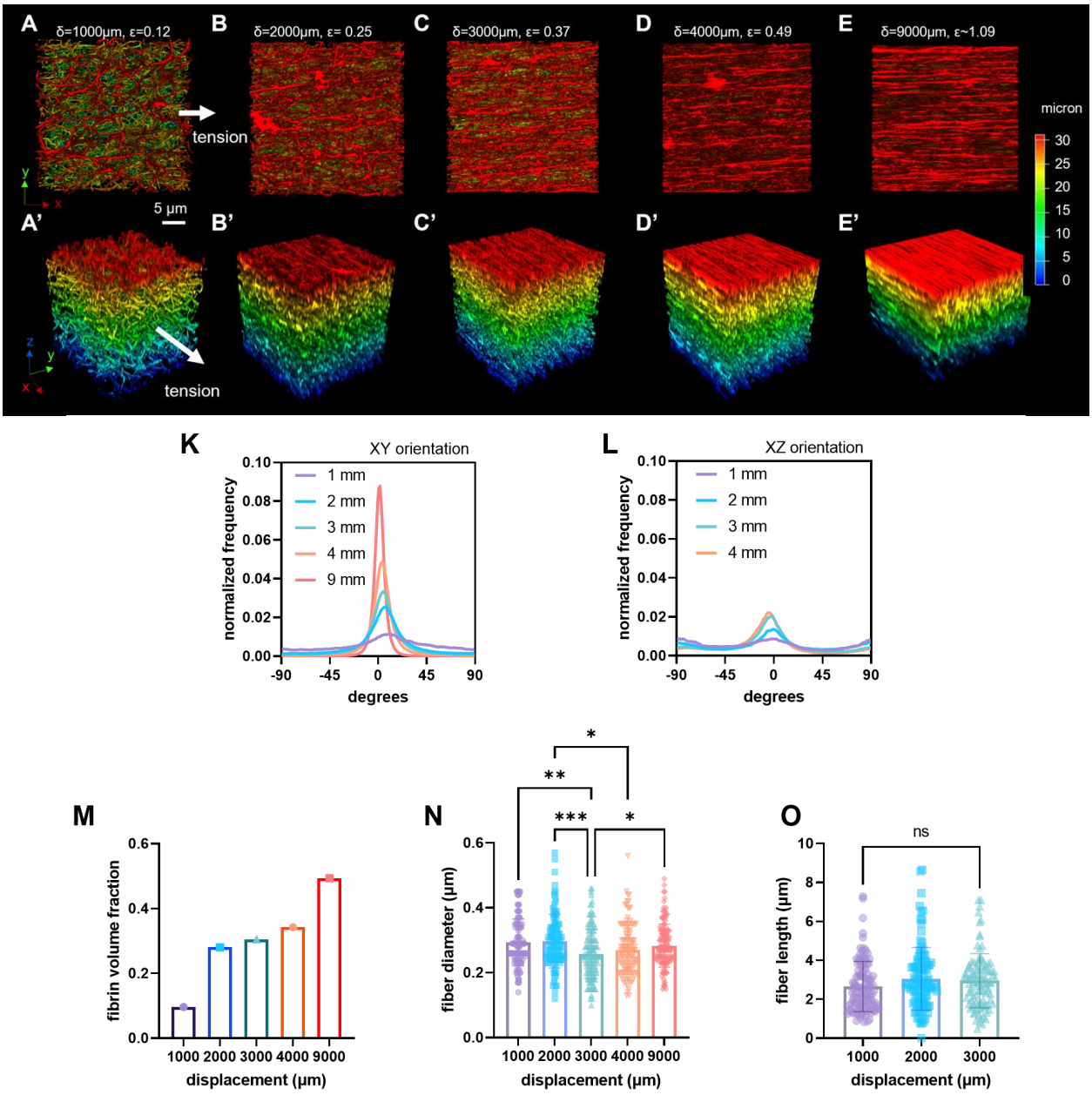

Figure 3.4. **Mesoscale characterization of 2 mg/mL fibrin gel network structure under uniaxial tension with the slider assembly.** Three dimensional renderings of fibrin gel displaced to δ = 1000, 2000, 3000, 4000, and 9000 μm with a (29 μm)^3 ROI. Top view, orthogonal to the XY plane (A-E) and isometric views (F-J). XY (K) and XZ (L) fiber orientations for different displacement values. (M) Fibrin volume fraction (n = 1) for different displacement values. (N) Average (±SD) fiber diameter (n=100) for δ = 1000- 9000 μm displacements. There were statistically significant fiber diameter differences between displacements from the one-way ANOVA ($p < 0.0001$). (O) Average (±SD) fiber length (n=100) for δ = 1000- 9000 μm displacements. There were no statistically significant fiber length differences between displacements from the one-way ANOVA ($p > 0.05$). All statistical analyses are from one-way ANOVA followed by Tukey's post hoc test, ns, $p > 0.05$, * $p < 0.05$, ** $p < 0.01$, *** $p < 0.001$.

The average and standard deviation for fiber lengths (n = 100) for δ = 1000, 2000, and 3000 μm was 2.66 ± 1.29 μm, 3.06 ± 1.62 μm, and 2.95 ± 1.39 μm, respectively (Fig. 3.4 O), without statistically significant differences as determined by the one-way ANOVA ($p > 0.05$). The resolution of these images, combined with increased fiber density, was not sufficient to confidently measure fiber lengths past the 3000 μm displacement configuration.

3.3 Heterogeneous Fibrin Gel with Varying Density

The ECM varies in composition, organization, and mechanical properties. ECM heterogeneities are apparent at the interfacial boundaries between a wound and healthy tissue or a tumor and its surrounding stroma. A heterogeneous fibrin construct was prepared to model a heterogeneous ECM boundary and demonstrate the characterization of non-uniform stress and strain during uniaxial tension. Confocal imaging of the heterogeneous fibrin gel showed a cohesive interface between the 2 mg/mL and 4 mg/mL fibrin (Fig. 3.5 A, B). Different local Green Lagrange strains were observed during tensile testing of this gel (Fig. 3.5 C-F). For the displacement shown, regions encompassing the 4 mg/mL fibrin experienced an average strain (± S.D.) of 0.29 ± 0.06. Notably, regions in the 2 mg/mL fibrin region, adjacent to the 4 mg/mL fibrin inclusion, experienced a higher average strain of 0.36 ± 0.02.

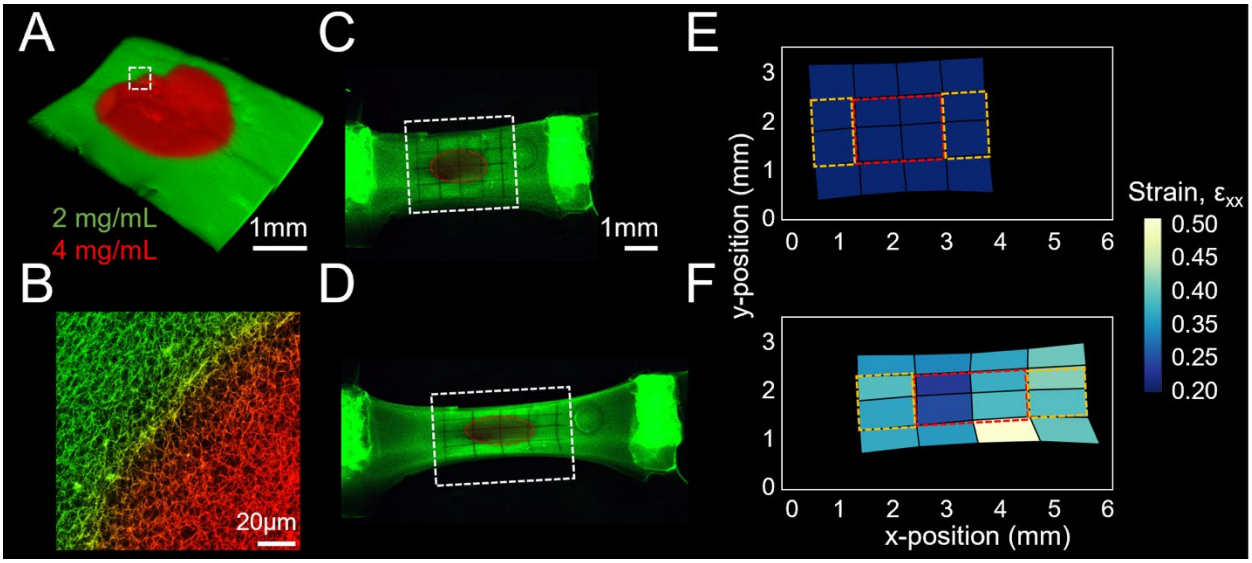

Figure 3.5. **Strain field of heterogeneous fibrin gel.** (A) 3D rendering and (B) microscale structure of 2 mg/mL fibrin (green) with a 4 mg/mL fibrin inclusion (red). Gel before (C) and during (D) tensile testing. Strain field before (E) and during (F) tensile testing. Regions encompassing and adjacent to the 4 mg/mL fibrin outlined in red and yellow, respectively.

The FE model defined from measurements from confocal imaging (Fig. 3.6 A) and with the macroscale mechanical properties from empirical data, showed consistent results with what was observed experimentally. The stress was nearly constant in the 4 mg/mL inclusion and the regions adjacent to it on the left and right side (Fig. 3.6 B). However, because the inclusion was made out of a stiffer material, the strain in the inclusion was smaller compared to the adjacent regions (Fig. 3.6 C), as observed experimentally. Position 1, within the 4 mg/mL fibrin, had a tangent modulus of 0.29 MPa at $\varepsilon = 0.25$. Position 2, within the 2 mg/mL fibrin had a tangent modulus of 0.15 MPa at $\varepsilon = 0.25$. The curves of the bulk 2 mg/mL and 4 mg/mL material are plotted for comparison (Fig. 3.6 D). The homogenized modulus of the heterogeneous fibrin gel was 0.18 MPa at $\varepsilon = 0.25$.

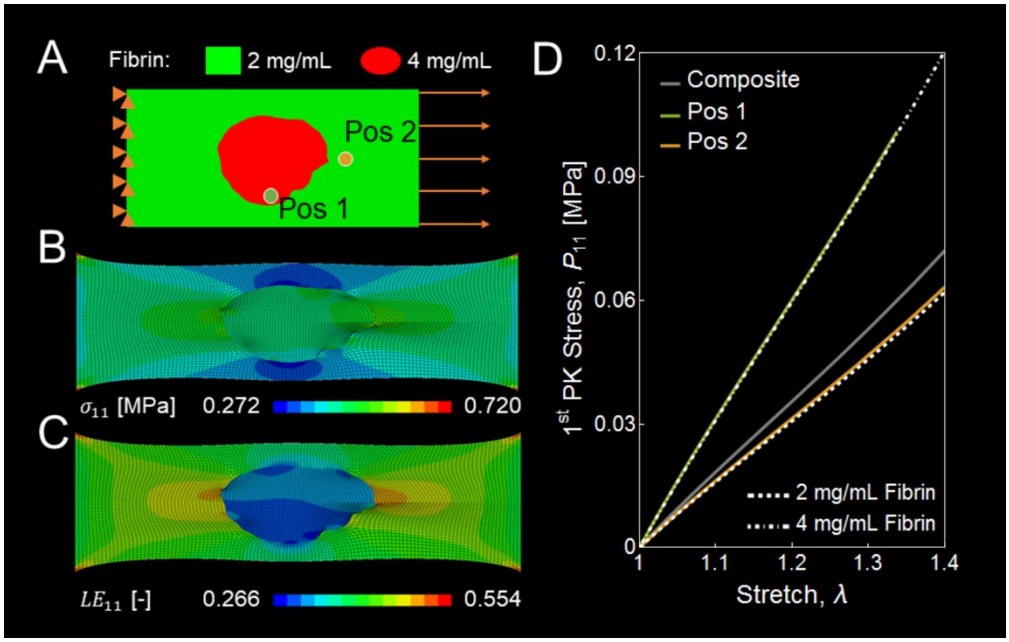

Figure 3.6. **Predictive computational model of heterogeneous fibrin gels. (**A) FE model of heterogeneous gel informed from mechanical characterization of homogeneous fibrin. Stress (B) and logarithmic strain (C) fields from FE model. (D) Local stress-strain response within (1) and adjacent (2) to the 4 mg/mL inclusion.

4. DISCUSSION

Here we propose and demonstrate empirical methods that can be used to analyze the macroscale mechanical properties and mesoscale structure of fibrin gels under uniaxial tension. Additionally, we demonstrate a strategy to characterize the non-uniform mechanical properties of heterogeneous fibrin gel constructs representative of interfacial ECM boundaries that vary in structure (*e.g.* wound or tumor). These methods can be expanded to characterize the mechanics of other biomaterials to inform computational models that seek to improve scaffolding designs for applications in improving the clinical output of wound healing and tissue regeneration after injury.

4.1 Macroscale Mechanical Characterization of Fibrin

Confocal imaging of homogeneous fibrin showed that fibril density increased with higher fibrinogen concentration (Fig. 3.1 C-E), which aligns with previous findings (Bruekers et al., 2016; Ryan et al., 1999).

Increase in stiffness with increasing fibrinogen concentrations has been previously reported (Piechocka et al., 2010; Ryan et al., 1999). The tangent average tangent moduli and standard deviation of the 2, 4, and 6 mg/mL fibrin at $\varepsilon = 0.25$ were 0.15 ± 0.08 MPa, 0.30 ± 0.16 MPa, and 0.71 ± 0.26 MPa, respectively (Fig. 3.1 B). The majority of mechanical information related to fibrin gel involves shear stress from rheological data. However, there are a few studies that evaluate uniaxial tension. These values can be compared to a tangent modulus of 2.5 kPa (Pathare et al., 2021) and 8 kPa (Sugerman et al., 2020) for whole blood clots under tension. The tangent modulus of 2 week-old 6.6 mg/mL fibrin gel under tension ranged from 0.06 ± 0.10 MPa to 0.12 ± 0.04 MPa (Sander et al., 2011). A tangent modulus of approximately 0.05 MPa at $\varepsilon = 0.25$ was measured for 0.08 mg/mL fibrin gel samples prepared from platelet-poor-plasma (Britton et al., 2019). In contrast, the stiffness of individual fibrin fibers under tension is 1.7 ± 1.3 MPa (Janmey et al., 2009).The stress-strain response of fibrin under tension in our experiments is observed to be linear, which is expected of fibrin gels stretched below $\varepsilon \approx 1.2$ (Brown et al., 2009). The viscoelastic properties of fibrin gels and whole blood clots have been documented through tensile testing and rheology (Münster et al., 2013; Sugerman et al., 2020). In this study we did not characterize the viscoelastic properties of fibrin gels. To further evaluate the viscoelastic properties

of fibrin gels, the following tests can be conducted on our macroscale and mesoscale imaging modalities: stress relaxation, tensile testing at different strain rates, and cyclic tensile loading and unloading with evaluation of hysteresis (Sugerman et al., 2020).

4.2 Mesoscale Mechanical Characterization of Fibrin

Static Configuration

For 2, 4, and 6 mg/mL fibrin gels polymerized in 3D printed molds, the orientation of fibers from the perspective of the XY plane, and relative to the longitudinal geometry of the gel (x-axis), was similar across all concentrations (Figure 3.2 I). There was no notable alignment in a particular orientation, indicating that the fibers were randomly aligned. In the XZ plane, relative to the longitudinal geometry of the gel (x-axis), there appeared to be a relative peak in alignment at the ±90° orientation, suggesting that fibers were aligned vertically (z-axis), across all fibrinogen concentrations (Figure 3.2 J). It is expected that in static configurations where there are no applied tensile loads, or fluid flow conditions, that the fiber alignment is isotropic (Chandrashekar et al., 2018; Wang et al., 2021). Since only isotropic alignment from the XZ plane under static conditions has been reported (Wang et al., 2021), imaging and analysis protocols will be reviewed to rule out the possibility of erroneous calculations. The trend in increased fibrin volume fraction with higher fibrinogen concentration (Fig. 3.2 K), has been previously observed, due to increased fiber density (Bruekers et al., 2016). There appeared to be a slight trend of decreasing fiber diameter with increasing fibrinogen concentration, with diameters for the 2 mg/mL gel being statistically greater than the fiber diameters of the 4 mg/mL and 6 mg/mL gels (Fig. 3.2 L). From the literature, there is a slight decrease in fibril diameter associated with increased fibrinogen concentration (Bruekers et al., 2016; Ryan et al., 1999). Fiber diameters were comparable to those from the literature, with average fiber diameters ranging from 0.210 – 0.270 μm measured with confocal microscopy (Bruekers et al., 2016) and individual fiber measurements ranging from 0.016 – 0.391 μm when done with SEM (Ryan et al., 1999). There was a slight trend in decreasing fiber length with increasing fibrinogen concentration. Particularly, fiber lengths for the 2 mg/mL gel were statistically greater than fiber lengths for the 6 mg/mL gel (Fig. 3.2 M). Similar trends have been observed before, the decrease in fiber length is attributed to the increase in fiber density, given limited volume, more branch points mean shorter fiber lengths (Ryan et al., 1999). Fiber length measurements were comparable to average fiber lengths ranging from 0.3 ± 0.2 μm to 4.8 ± 3.5

μm made with SEM (Ryan et al., 1999). These characterizations were made from single samples (n = 1) of each fibrinogen concentration. To more accurately capture the variations from the expected heterogeneity of biological samples and differences in experimental conditions during fibrin polymerization (*e.g.* temperature, pH, ionic concentrations), higher sample sizes of each fibrinogen concentration will need to be characterized.

Configuration Under Tension

The configuration of 2 mg/mL fibrin gels under increasing displacements was imaged and analyzed using the FemtoTools micromanipulator coupled with either a spring or slider. Slight undulations of liquid within the PBS retention well of the spring resulted in motion artifacts, particularly at higher magnifications using a 63x objective. Fiber alignment in the direction of tension (Fig. 3.3L, Fig. 3.4K, Fig. 3.4L) aligns with previous findings (Brown et al., 2009; Wang et al., 2021). The normalized frequency of fiber orientation in the direction of tension for the spring and slider in a 2 mg/mL fibrin gel were comparable to previous findings from a 5 mg/mL fibrin gel (Wang et al., 2021). The fibrin volume fraction was observed to decrease as a tensional displacement increased for both the spring (Fig. 3.3 M) and slider (Fig. 3.4M) assemblies. This observation supports previous findings of increased fibril density and decrease in relative volume (*i.e.* current volume divided by initial volume) as fibrin fibers align and bundle together when strain is applied (Brown et al., 2009). Using the FemtoTools and slider assembly, there were statistically significant differences in the fiber diameters as displacement increased from δ = 1000 – 9000 μm (Fig. 3.4 N). There was a trend of lower displacements having slightly larger diameters (*e.g.* δ=1000 μm > δ=3000 μm, δ=2000 μm > δ=3000 μm, δ=2000 μm > δ=4000 μm). This aligns with findings that tensile loads cause fiber diameters to decrease (Brown et al., 2009). It is interesting that 2 mg/mL fibrin fiber diameters imaged with 63x objective (static and slider) on average were approximately 0.29 μm thick. whereas those imaged with a 25x objective (spring) were approximately 0.38 μm. This could be an effect of biological and experimental variability, or it could be related to the accuracy of resolution between magnifications. The voxel sizes for 63x and 25x magnification were 0.0253 μm x 0.0253 μm x 0.2812 μm (x y z) and 0.0722 μm x 0.0722 μm x 0.5054 μm (x y z), respectively. Comparing fiber diameters of the same sample using the 25x and 63x objective would be informative here. Fiber lengths were defined as the path between two branch points. Measuring fiber lengths from the acquired z-stacks was challenging as with

increasing displacement because it became increasingly difficult to identify branching points as fiber density increased, fibers overlapped, and fiber orientation converged towards the direction of tension. There were no statistically significant differences among fiber lengths that could be discerned for $\delta = 1000 – 3000$ μm using the slider assembly (Fig. 3.4 O). However, it is worth noting that fiber lengths measured were not biased based on fiber orientation, thus both fibers aligned and not aligned with the direction of tension were measured. An assessment of fiber length categorized by fiber orientation, would be necessary to evaluate if fibers in alignment with the direction of tension have different lengths than those in the direction of tension as displacement increases. Stress and strain information from the FemtoTools and spring assembly (Fig. 3.3 A-J, K) can be coupled with the structural network information gathered from the spring assembly (Fig. 3.3L-N) and slider assembly (Fig. 3.4 K-O) to inform discrete fibrin network computational models that seek to describe and predict how mesoscale structural properties influence macroscale mechanics. Future analysis could also inform on the branching density (number of fibers connected at a branch point), and branch point density (number of branch points for a given volume) as these are descriptive of the network structure (Britton et al., 2019; Ryan et al., 1999). The macroscale mechanical information and mesoscale structural parameters that we have collected here (*i.e.* volume fraction, fiber diameter, fiber length, fiber orientation), will be used to inform a DFN computational model. Informing DFNs with tensile stress-strain data and mesoscale structural deformations from the same sample has not been achieved until now. The DFN will be able to run multiple simulations predicting how altering the structural parameters of fibrin gels would influence the macroscale mechanical properties. This computational model will speed up the development of scaffolding with desired structural and mechanical properties by optimizing design parameters through simulations, which are fast faster than experimental approaches.

Future work will aim to minimize motion artifacts from the FemtoTools and spring system by increasing the stability of the sample interface. One approach would be to update the spring model, which has a stiffness low enough to resolve the force contribution of fibrin gels, to be more stable by incorporating low friction railings that prevent off-axis movement, or by utilizing more stiff materials, such as the silicon wafers used in other hydrogel tensile testing platforms (Elhebeary et al., 2019; Emon et al., 2021). Another approach would be to reduce the force contribution of friction from the slider system. Mineral oil (Lily White, AlbaChem) was used to lubricate the slider, but did not reduce the friction enough to resolve the force contribution of fibrin

gels with this setup. Other commercially available lubricants and sliders can be tested. Additionally, image acquisition optimization and image post-processing and analysis to characterize network properties will be explored.

4.3 Heterogeneous Fibrin Gel with Varying Density

A heterogeneous fibrin gel composed of 2 mg/mL fibrin with a 4 mg/mL ellipsoid insert (Fig. 3.5 A, B) was constructed to model an interfacial ECM boundary with different material properties. The heterogeneous fibrin gel had a non-uniform strain distribution that varied by region upon tensile testing. As expected, regions with higher concentration experienced a lower strain than regions composed of the lower concentration fibrin. This is supported by both the empirical data (Fig. 3.5 E, F) and FE model simulated strain fields (Fig. 3.6 C). Creating an FE model based on the mechanical properties of homogeneous fibrin allowed us to simulate the stress-strain response of heterogeneous gels that was verified experimentally. The overall stress-strain response of heterogeneous gel, estimated from the FE model, falls in between the bulk response for the 2 mg/mL and 4 mg/mL fibrin. Notably, the strain field for the heterogeneous gel was measured experimentally by imaging the deformation of a fiducial grid. These results aligned with the FE model. The heterogeneous fibrin gel model demonstrated here with a stiff inclusion could be representative of tumor ECM which is more stiff than the ECM of the surrounding stroma (Bordeleau et al., 2013). Adapting this model to have a an inclusion that is less stiff than its surrounding could be representative of a cutaneous skin wound in which a softer fibrin clot is surrounded by a stiffer, mostly collagenous, healthy tissue (Miron-Mendoza et al., 2017). Additional configurations could be modeled to create *in vitro* models with material composition and geometric complexity more representative of *in vivo* ECM conditions.

5. CONCLUSIONS AND FUTURE WORK

In summary, we demonstrated a strategy to quantify the multiscale mechanics of fibrin gels by measuring the macroscale stress-strain response and the mesoscale fiber network structure during uniaxial tensile tests. Information gathered from these tests can be used to inform computational models that seek to describe and predict how structural changes of the ECM at the mesoscale influence macroscale stress and strain, and vice versa. Future iterations of our mechanical testing setup will seek to minimize minute sample movements that may lead to motion artifacts in acquired images. We also developed an *in vitro* model using heterogeneous fibrin gels to recapitulate an interfacial ECM boundary. We informed a computational model with the empirical stress-strain response and organization of homogeneous fibrin gels. The model was then used to predict the non-uniform stress and strain of the heterogeneous gel under uniaxial tension. Future work may also include making these *in vitro* models more physiologically relevant by incorporating additional factors that influence multiscale mechanics of the ECM such as cell-regulated ECM degradation and deposition in response to mechanical and biochemical stimuli. The strategies proposed here can be extended to characterize the multiscale mechanics of other biological materials and improve scaffold design, including complex interfacial ECM boundaries between tissues.

APPENDIX A – DESIGN AND VALIDATION OF A MODULAR MICRO-ROBOTIC SYSTEM FOR THE MECHNICAL CHARACTERIZATION OF SOFT TISSUES

Design and validation of a modular micro-robotic system for the mechanical characterization of soft tissues

Andrea Acuna[a]
Julian M. Jimenez[a]
Naomi Deneke[b]
Sean M. Rothenberger[a]
Sarah Libring[a]
Luis Solorio[a,c]
Vitaliy L. Rayz[a]
Chelsea S. Davis[b]
Sarah Calve[a,d,*]

[a]Weldon School of Biomedical Engineering, Purdue University, 206 South Martin Jischke Drive, West Lafayette, IN 47907
[b]School of Materials Engineering, Purdue University, Neil Armstrong Hall of Engineering, 701 West Stadium Avenue, West Lafayette, IN 47907
[c]Purdue Center for Cancer Research, Purdue University, 201 South Street, West Lafayette, IN 47906
[d]Paul M. Rady Department of Mechanical Engineering, University of Colorado – Boulder, 1111 Engineering Center, 427 UCB, Boulder, CO 80309

*Corresponding author: Prof. Sarah Calve,
Prof. Sarah Calve, Tel: +1 (303) 492-7604, E-mail: sarah.calve@colorado.edu

Abstract

The mechanical properties of tissues are critical design parameters for biomaterials and regenerative therapies seeking to restore functionality after disease or injury. Characterizing the mechanical properties of native tissues and extracellular matrix throughout embryonic development helps us understand the microenvironments that promote growth and remodeling, activities critical for biomaterials to support. The mechanical characterization of small, soft materials like the embryonic tissues of the mouse, an established mammalian model for development, is challenging due to difficulties in handling minute geometries and resolving forces of low magnitude. While uniaxial tensile testing is the physiologically relevant modality to characterize tissues that are loaded in tension *in vivo*, there are no commercially available instruments that can simultaneously measure sufficiently low tensile force magnitudes, directly measure sample deformation, keep samples hydrated throughout testing, and effectively grip minute geometries to test small tissues. To address this gap, we developed a micromanipulator and spring system that can mechanically characterize small, soft materials under tension. We demonstrate the capability of this system to measure the force contribution of soft materials, silicone, fibronectin sheets, and fibrin gels with a 5 nN – 50 μN force resolution and perform a variety of mechanical tests. Additionally, we investigated murine embryonic tendon mechanics, demonstrating the instrument can measure differences in mechanics of small, soft tissues as a function of developmental stage. This system can be further utilized to mechanically characterize soft biomaterials and small tissues and provide physiologically relevant parameters for designing scaffolds that seek to emulate native tissue mechanics.

Keywords

Tensile testing, soft tissue mechanics, tendon mechanics, embryonic tendon, extracellular matrix

Statement of Significance

The mechanical properties of cellular microenvironments are critical parameters that contribute to the modulation of tissue growth and remodeling. The field of tissue engineering endeavors to recapitulate these microenvironments in order to construct tissues *de novo*. Therefore, it is crucial to uncover the mechanical properties of the cellular microenvironment during tissue formation. Here, we present a system capable of acquiring microscale forces and optically measuring sample deformation to calculate the stress-strain response of soft, embryonic tissues under tension, and easily adaptable to accommodate biomaterials of various sizes and stiffnesses. Altogether, this modular system enables researchers to probe the unknown mechanical properties of soft tissues throughout development to inform the engineering of physiologically relevant microenvironments.

1. Introduction

Biological tissues perform a myriad of functions and vary broadly in composition and mechanical properties. The extracellular matrix (ECM) is an essential component of tissues and is a dynamic network of macromolecules that surrounds cells, regulates cellular behavior, and provides a substrate for tissue organization[1]. The composition of the ECM and interactions between cells and the ECM contribute to the mechanical functionality of tissues[2,3]. Conversely, the mechanical environment is an important factor that drives cellular function and organization[4,5]. Age and disease significantly influence the material properties of biological tissues. Mechanical characterization can assess how these factors change tissue functionality[6,7]. For instance, during tendon development, the composition and organization of the ECM and cells vary widely, which will manifest in changes in the mechanical response of the tissue, such as an increase in tensile strength and tangent modulus[8,9]. Mechanical cues from tissue stiffness, muscle contractions, and embryonic motility support tendon development and changes in material properties (e.g., tangent modulus), which affect the effective transfer of force from muscle to bone, directly impacting functionality[10].

Given the parallels between embryonic development and effective wound healing, understanding how mechanical changes correlate with cell and ECM dynamics during embryonic development can inform tissue engineering and regenerative medicine strategies[11,12]. Mice are commonly used in the study of development and disease due to the ease of genetically modifying the expression of proteins of interest compared to other mammalian species[13–15]. Due to the challenges in mechanically testing embryonic murine tendons, tendon development has been studied using chick models and indentation force curves from tendon cryosections to calculate the moduli at the nano and microscales[16,17]. The microscale moduli increased nonlinearly during

development, ranging from ~10-150 kPa; however, other values reported in the literature for the moduli of late-stage embryonic chick tendon undergoing uniaxial tensile loading varied by about 100-fold, ranging from 0.21 MPa to 20 MPa [10,18]. The use of cryosections limits the evaluation of whole-tissue mechanics as a function of development and does not replicate the physiological loading conditions of the tendon *in vivo*. While cell-scale mechanical properties may be more relevant in investigating mechanoregulation of cell differentiation and function, studying the macroscale tensile properties of embryonic tendon is critical for understanding tissue mechanics as a function of development.

Additionally, *in vitro* models are a powerful tool to understand the mechanical interactions between cells and the ECM at the fibrillar scale, required to ensure appropriate cell behavior and tissue function[6,19,20]. The use of multifunctional ECM polymers like fibrin and fibronectin provides a framework for evaluating the ECM at the fibrillar scale; however, the mechanical influence of these polymers during tissue growth and remodeling is not completely understood. Fibrin is a temporary matrix that supports blood clotting and wound healing *in vivo*. Gels can be made *in vitro* by combining fibrinogen and thrombin, and fibrin gel is used in the clinic as a wound sealant due to its quick polymerization reactions and appropriate tissue adherence. Fibrin gel has also been used as a scaffold in tissue engineering applications[21]. Fibronectin is an ECM protein with many roles, including facilitating cellular adhesion and migration through the ECM, tissue growth and development, and ECM assembly[22]. Under the right conditions *in vitro*, fibronectin can be polymerized into robust sheets for the 3D culture of cells[23,24]. Characterization of the mechanical properties of embryonic murine tissues and ECM polymers is crucial for understanding the role of mechanics in tissue assembly and providing a benchmark for *de novo* functional tissue formation and applied regeneration strategies[25,26].

Nevertheless, the mechanical characterization of murine soft tissues and ECM polymers is challenging due to difficulties in handling samples with small dimensions and measuring forces of low magnitudes, making tensile testing equipment used for adult soft tissues unsuitable. Additionally, synthetic hydrogels can be difficult to generate in large geometries to mechanically test using traditional uniaxial tensile testing instrumentation, despite being a critical step in the evaluation of biomaterials[27–29]. Atomic force microscopy (AFM) indentation measurements can be used to mechanically characterize materials and has been utilized to study tissues and hydrogels at the nano and microscales [30]. Using AFM to measure stiffness through compression is a suitable testing modality for hydrogels and other biomaterials designed to withstand compressive forces, for instance, when seeking to recapitulate cartilage. However, many tissues are loaded in tension *in vivo*, such as tendon, and cells exert tensile forces onto their surrounding microenvironment so that ECM networks and fibrils are uniaxially loaded[31]. The ability to test small, soft tissues and biomaterials in tension while taking force measurements is therefore critical for identifying parameters for regenerative therapies.

Various commercially available and custom-built systems have been developed to uniaxially test small biological materials in tension. The length of small, soft materials that have been tested can range from 500 μm[32] for hydrogels to 20 mm for adult rat Achilles and tail tendon fascicles[33]. The force threshold and resolution that can be measured depend on the sensing mechanism. For example, different uniaxial tensile testing systems used to characterize soft biomaterials or tissues had force resolutions (i.e., the minimum force magnitude that can be measured with a system) ranging from 11 nN[32] to 2.5 mN[34] with force thresholds of at least 100 μN to 2500 μN, respectively. Other commercially available and custom tensile testing systems relevant to biomaterials include: BioTense Bioreactor (Admet) with a 5 N force threshold and 1000

μN resolution; UStretch (CellScale) and Biotester (CellScale) with 0.5 N threshold and 1000 μN resolution; Material Testing System developed by Ye et al.[35] with 0.2 N threshold and 100 μN resolution; MicroTester (CellScale) with 5 μN threshold and 10 nN resolution. Securing soft biological samples via clamps or winding with wire or thread in order to secure them for testing can result in stress concentrations, increased local deformation proximal to the grips, and low friction between clamps and the sample that can lead to slipping[27,36,37]. Grip-to-grip displacement can be used to calculate strain; however, this does not capture regional variation or account for deformation at the interface between the tissue and the grips. Therefore, strain is commonly calculated by tracking the displacement of the sample of interest using optical surface markers (e.g., microspheres, graphite)[33,38,39] to directly observe sample deformation, avoiding errors attributed to gripping soft biological materials.

Currently available uniaxial tensile testing modalities meet some of these desirable specifications. However, there is no single system that possesses all the necessary criteria to mechanically characterize mouse embryonic tendons. There is a need for an instrument that can measure force at sufficiently high resolution, optically measure sample deformation, keep samples hydrated throughout testing, and effectively secure the minute geometries of embryonic mouse tendons and other small, soft tissues and biomaterials. To address this gap, we developed a system that satisfies all these criteria. We designed and 3D printed springs and fabricated sample holding frames to accommodate a range of sample geometries and stiffness. The spring was coupled with a commercially available micromanipulator and force sensors (FemtoTools) that have 100 μN threshold with 5 nN resolution, 10,000 μN threshold with 5 μN resolution, and 100,000 μN threshold with 50 μN resolution (depending on the sensor used and the data acquisition rate), and with a dissecting microscope to visualize sample deformation. The FemtoTools system was chosen

because it provides force thresholds and resolutions comparable to other commercially available tensile testing modalities relevant to biomaterials. Additionally, the modularity of the FemtoTools system allowed us to adapt our system to accommodate different sample sizes and stiffnesses. The system was validated by comparing the measured mechanical response of Solaris Silicone, a material with known mechanical properties, to the mechanical response of the same material measured with a commercially available tensile tester. Our system measured the mechanical responses of soft materials of varying stiffnesses and geometries, including fibronectin sheets, and fibrin gels, as well as assess mouse embryonic tendon mechanics as a function of development. This system can be further utilized to mechanically characterize other tissues and ECM, which is critical for expanding the understanding of the cellular microenvironment during growth and development and defining design parameters for scaffolding with applications in regenerative medicine.

1. Materials and methods

1.1. Development of modular tensile testing system

The micromechanical testing assembly was built around a dissecting microscope (M80, Leica Microsystems; Fig. 1A). A commercially available micromanipulator system (FT-RS1002, FemtoTools) and force sensing probes (FT-S10'000 and FT-S100'000, FemtoTools) were adapted for uniaxial loading of small soft tissues and biomaterials (Fig. 1B). The micromanipulator system maneuvers along the *x*, *y*, and *z* axes with a displacement range of 5 nm – 26 mm. The microforce sensing probes are capable of resolving 5 nN – 50 μN forces. The micromanipulator and each individual microforce sensor were calibrated by the manufacturer prior to use. The displacement of the micromanipulator was verified optically under a dissecting microscope. The microforce

sensors have exposed electronics that can be damaged when they come in contact with aqueous solutions. Therefore, springs were designed to act as an interface that allows samples to remain hydrated during testing, while providing an attachment point for the microforce sensor away from the liquid.

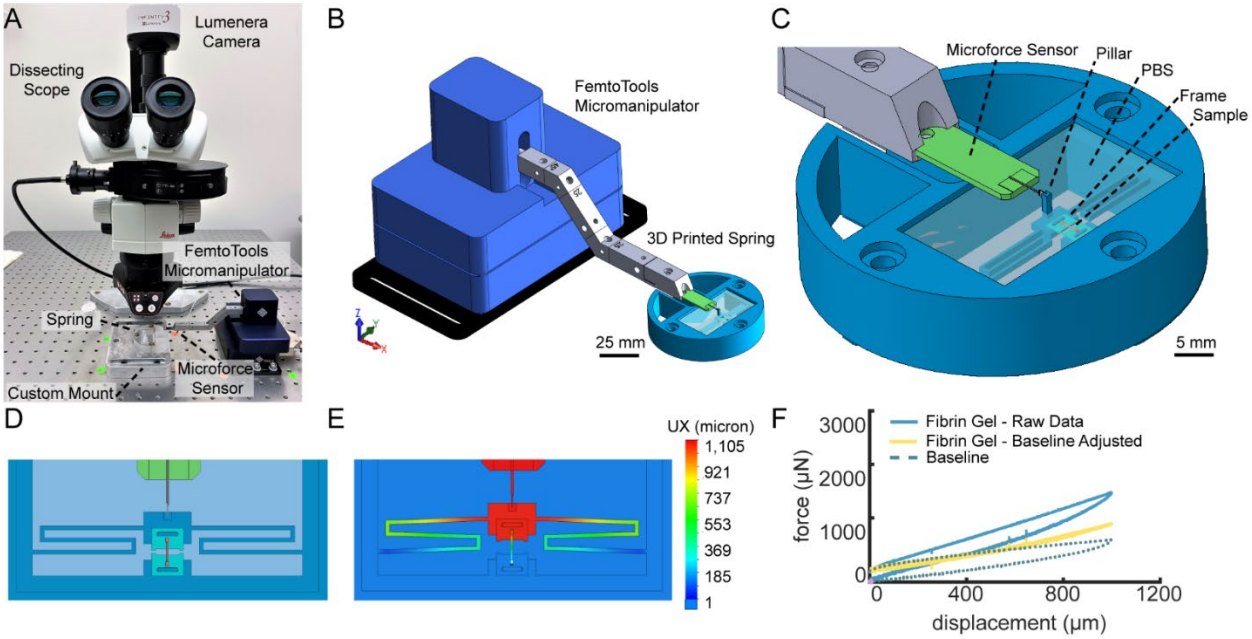

Figure 1. Instrumentation to measure force and optical displacement of soft tissues. (A) Dissecting microscope and mechanical testing system. (B) FemtoTools micromanipulator and spring assembly. (C) Detail of spring assembly. The microforce sensor has a custom hook probe that connects the micromanipulator to the spring, enabling the samples to remain hydrated in PBS. Samples are glued onto frames and loaded onto the spring. The sides of the frame are cut prior to testing. Top view of SolidWorks model of sample before (D) and during (E) tensile testing. (F) Fibrin gel raw data, baseline, and baseline-adjusted force-displacement curves demonstrate the ability of the system to measure the force contribution of soft materials. At a displacement of 1000 µm, the force values for the raw fibrin gel, the baseline adjusted fibrin gel, and the baseline were 1478 µN, 899 µN, and 579 µN, respectively. At a 1000 µm displacement, the raw fibrin gel force was 155% greater than the respective baseline value at the same displacement.

Custom springs and frames (Fig. 1C) were designed and fabricated to accommodate the mechanical testing of samples with varying geometries and stiffnesses. Three spring configurations, spring 1, spring 2, and spring 3, were designed to accommodate different sample

geometries by varying the distance between fixed and moveable ends (Supplemental Fig. 1). The distance between the fixed and moveable end was 2 mm, 3.7 mm, and 8.5 mm for spring 1, spring 2, and spring 3, respectively. Frames were drawn in Adobe Illustrator (Adobe) and laser cut out of 100 μm-thick polyethylene terephthalate (PET) using a Universal Laser VLS3.50 (Universal Laser Systems) (Supplemental Fig. 2A-H). The PET frames kept the samples in a static configuration and minimized sample deformation while staining, processing, and mounting onto the 3D printed springs. The spring and micromanipulator assembly were securely mounted onto an optical table using custom-built fixtures to avoid undesired part movement during testing and consequent system damage. The dissecting microscope, also securely mounted on the optical table, facilitated handling and situating samples on the 3D printed spring and enabled the calculation of optical strain.

Springs were designed using SolidWorks (Dassault Systèmes), 3D printed (ProJet MJP 2500) with UV curable plastic (M2R-CL, VisiJet), and post-processed to remove wax support material by placing first in a steam bath then a heated oil bath, following the manufacturer's guidelines. The resolution of the printer is 32×28×32 μm^3. A liquid-retention basin was incorporated into the spring design to keep samples hydrated with 1× phosphate buffered saline (PBS) throughout testing. The spring was connected to the micromanipulator system via a pillar that vertically offset the microforce sensor, away from the PBS, to minimize risk of damaging exposed electronics (Fig. 1C). The resolution of the 3D printer was not sufficient to create an interface onto which the hook at the end of the microforce sensor probe could attach. Therefore, a small PET hook-interface was laser cut and adhered onto the spring at the top of the pillar using Loctite Super Glue Gel Control (cyanoacrylate-based adhesive). The PET hook-interface was designed to facilitate attachment to the hooked probe at the end of the microforce sensor (Fig. 1C).

The initial force-displacement measurement was compared to other springs to confirm the mechanical response was within the expected magnitude.

1.2.Mechanical Testing Protocol

PBS was added to the liquid-retention basin of the spring at least 2 hours prior to mechanical tests. PET frames containing the samples to be tested were manually loaded onto the spring and cut with angled scissors prior to mechanically testing (Supplemental Fig. 2A-H), freeing the sample to deform under tension. (Fig. 1C-E). The length of each sample was measured optically and was used to calculate the appropriate speed to achieve the desired strain rate. Custom LabVIEW programs were written to control the movement of the micromanipulator and to automate testing by prescribing the direction, magnitude, and speed of displacement. Force measurements and actuator displacement were recorded at 100Hz. Force-displacement curves were used to demonstrate the capability of the system to measure the force response of soft materials. To further characterize the stress-strain response of certain specimens, strain and cross-sectional area were measured optically.

To enable the optical measurement of engineering strain, fiducial lines were photobleached onto AF488 labeled specimens using an upright Zeiss LSM 800 confocal microscope (Carl Zeiss Microscopy) and a 10× Plan-Neofluar (NA = 0.3) objective. Equidistant lines were photobleached by creating a 20 μm wide region of interest (ROI) along the sample width using the *Crop* feature in the ZenBlue software package (Carl Zeiss Microscopy). The power of the 488 laser was set to 100% and a line was photobleached into the AF488 stained samples by acquiring a z-stack through the sample thickness in 10 μm increments. After the photobleached lines were generated, a z-stack of the entire sample was acquired (Supplemental Fig. 2I-K). The unloaded cross-sectional area

was measured between each pair of fiducial lines from the z-stack acquired using the ZenBlue software package (Carl Zeiss Microscopy).

The dissecting microscope magnification was adjusted to enable visualization of the sample throughout testing and a camera (INFINITY3-3URC, Lumenera) was coupled to the microscope to acquire videos for the duration of a mechanical test. For 2.5× magnification, the ROI during video acquisition was 6.2 mm × 4.7 mm and 1936 × 1456 pixels. The exposure time was adjusted for each sample to optimize contrast between the sample and fiducial lines using the camera's software package (INFINITY ANALYZE 6.5, Lumenera). Frame rate is inversely proportional to exposure time. Since the exposure time was adjusted for each sample based on fluorescence intensity, the frame rate ranged from 3 – 8 frames/second.

The spring and sample were loaded in parallel (Fig. 1C). Parallel force contributions are additive, i.e., $F_{combined} = F_{spring} + F_{sample}$. Therefore, to isolate the force contribution of the sample, the contribution of the spring, or baseline, was measured prior to every test by recording force-displacement data of the spring in the system without a sample (Fig. 1F). A baseline was recorded for each individual sample at the appropriate strain rate (based on the sample length) and to account for potential variation in the force contribution of the spring over time.

1.3.Data analysis

After tensile testing was completed, the baseline force readings (i.e., spring alone) were subtracted from the force recorded for each sample to isolate the force contribution of the material of interest (i.e., $F_{sample} = F_{combined} - F_{spring}$). To calculate stress, the isolated force for each sample was divided by the cross-sectional area. The FIJI (NIH) *getSplineCoordinates* macro was modified and used to manually draw segmented polylines over the fiducial lines on each frame from the recorded video. Each polyline was converted into a smoothed spline, and the x and y position of

each point along the splines was output as an array on a .txt file. A custom MATLAB (MathWorks) algorithm was written to import the output arrays from FIJI and calculate the average distance between fiducial lines for each frame from the recorded video using the *x* and *y* coordinates from the FIJI output. Optical strain was calculated using the equation $(L_i - L_0)/L_0$, where L_0 is the average distance between fiducial lines for the first frame of the video, and L_i is the average distance between fiducial lines for each subsequent frame (Supplemental Fig. 3).

The acquisition rate for force measurement was 100 data points per second (100Hz), and videos were recorded at 3 – 8 frames per second. Therefore, the stress data arrays were larger and contained more time intervals than the strain data arrays. To generate stress-strain curves, a time array was generated using the strain data. Then, stress values which corresponded to the strain time points were selected. The corresponding stress and strain data were plotted and fit to a polynomial function using Excel curve fitting algorithms, based on R^2 values, ensuring the polynomials followed the typical stress-strain responses of soft tissues[40,41]. The derivative of the polynomial function at a specific strain value was used to calculate the tangent moduli at selected strains.

1.4.Sample preparation

1.4.1. Reference material – Solaris silicone

System validation was performed by testing Solaris (Smooth-On, Inc.), a platinum-cured silicone, and comparing data from our setup with that acquired using a commercially available bulk tensile tester (TA.XT*Plus* Connect, Stable Micro Systems). Solaris was selected because it has well defined material properties that can be modulated to be similar to the biological samples of interest[27,42,43]. Solaris was prepared per manufacturer's instructions and cut to size manually with a scalpel blade. A mixture of equal parts Solaris Part A and Part B was prepared in a 20 mL scintillation vial followed by degassing with a vacuum desiccator. Thin film samples for

mechanical testing on the FemtoTools system were prepared by spin coating (Laurell Technologies Corporation WS-650-23B) 2 g of uncured Solaris on a 75 mm × 25 mm microscope slide coated with polyacrylic acid, which served as a sacrificial layer. Samples were spin coated at 3000 RPM for 30 seconds then placed in an oven at 70ºC to cure for 3 hours. The films were removed from the microscope slide by dissolution of the intermediate polyacrylic acid layer using reverse osmosis purified water. To generate samples with the optimal aspect ratio (length:width $\geq$ 5:1) for tensile testing, the thin films were cut using a laser-etched grid and a scalpel[44,45]. The resulting dimensions were measured optically from images acquired with a dissecting microscope. Samples tested with spring 1 were 2645.0 ± 471.4 µm × 216.4 ± 42.3 µm (n = 5) and samples tested with spring 2 were 3514.0 ± 420.6 µm × 308.1 ± 82.5 µm (L × W) (n = 5), all with a thickness of 117.0 ± 4.2 µm. Solaris thin films were adhered directly to PET frames using Loctite Super Glue Gel Control (Supplemental Fig. 2E). Tensile tests were performed using the FemtoTools micromanipulator and spring system described above, while the samples were surrounded by PBS. Tensile tests were conducted using spring 1 and spring 2. Actuator displacement data was used to calculate strain.

1.4.2. Bulk material testing – Solaris silicone

Samples for bulk testing were prepared by filling a 75 mm × 50 mm × 4 mm glass mold with uncured Solaris and leaving it to cure in an oven at 70ºC for 5 hours. The dimensions of samples tested on the bulk tensile tester were 15.29 ± 0.48 mm × 6.32 ± 1.50 mm × 3.85 ± 0.04 mm (L × W × H) (n = 5). For bulk testing, Solaris samples were gripped at each end using the TA.XT*Plus* clamps, and tensile tests were performed at a strain rate of 0.01 s^{-1} while force and displacement data were recorded through the TA.XT*Plus* Connect system. These tests were

performed in the ambient environment (i.e., dry) as it was not possible to add a hydration chamber around the TA.XT*Plus* Connect.

1.4.3. Fibrin gels

Porous polyethylene blocks were adhered onto 6 mm × 12.5 mm frames using Loctite Super Glue Gel Control and used as anchor points for 2 mg/mL fibrin gel constructs (Supplemental Fig. 2F). A custom mold was used to align the frame and to control the shape of fibrin gel as it polymerized so that a rectangular gel formed between the two porous polyethylene blocks. Human fibrinogen (14.15 mg/mL; FIB3, Enzyme Research Laboratories) and Alexa Fluor 488 conjugated human fibrinogen (1 mg/mL; F-13191, Molecular Probes) were thawed in a 37°C water bath, mixed at a 1:10 fluorescent to non-fluorescent fibrinogen content ratio, and diluted in PBS to achieve a 2 mg/mL fibrinogen solution. Next, 1 μL 2M $CaCl_2$ was added to the fibrinogen solution to increase gel rigidity and stability[46,47]. Human α-thrombin (HT 1002a, Enzyme Research Laboratories) was thawed, diluted to 1 U/μL, and added to the 2 mg/mL fibrinogen solution at a concentration of 0.0004 U thrombin per mg fibrinogen to initiate polymerization of the fibrin gel. Fiducial lines were photobleached and cross-sectional areas were measured as described above, however a STELARIS 5 confocal microscope (Leica Microsystems) and a 10x Apochromatic dry (NA = 0.40) objective were used. Frames with fibrin gels (n = 5) were loaded onto spring 3, and tensile tests were conducted at 0.01 s^{-1} strain rate and prescribing a 1000 μm – 6000 μm displacement, equivalent to $\varepsilon = 0.15 – 0.91$ based on actuator displacement. Samples were kept hydrated by PBS in the liquid-retention basin during testing.

1.4.4. Fibronectin

Polydimethylsiloxane (Sylgard 184, Dow Corning) was cured at a 10:1 elastomer to curing agent ratio, manually cut into 1 mm × 1mm × 1 mm blocks, adhered onto 6 mm × 12.5 mm PET

frames using Loctite Super Glue Gel Control, and coated with fibronectin sheet as previously described (Supplemental Fig. 2G)[23,48]. To visualize the samples, fibronectin-coated frames were stained with Alexa Fluor 488-conjugated wheat germ agglutinin (WGA; ThermoFisher), diluted 1:100 in 1× PBS + 0.2% bovine serum albumin + 0.02% sodium azide for 24 hours at 4°C, then rinsed with 0.1% Triton X-100 in 1× PBS (PBST) at room temperature for 30 minutes. Fibronectin-coated frames (n = 2) were loaded onto spring 3 for uniaxial loading and surrounded by PBS during testing. Cyclic loading was performed to 400 μm at a strain rate of 0.04 s^{-1} for 10 cycles. Tensile test to failure was conducted at 0.04 s^{-1}.

1.4.5. Developing tendons

All murine experiments were approved by the Purdue Animal Care and Use Committee (PACUC; protocol 1209000723). PACUC ensures that all animal programs, procedures, and facilities at Purdue University adhere to the policies, recommendations, guidelines, and regulations of the USDA and the United States Public Health Service in accordance with the Animal Welfare Act and Purdue's Animal Welfare Assurance. C57BL/6 mice were time-mated to generate embryonic day (E)16.5 and E18.5 embryos. Dams were euthanized via CO_2 inhalation, which was confirmed using cervical dislocation. Embryos were removed from the uterine horns, rinsed in chilled 1× PBS and the hindlimbs were excised at the hip joint. Tibialis anterior (TA) muscle-tendon-bone units were dissected by removing the skin with tweezers and then the surrounding connecting tissue with a blade under a dissecting microscope to avoid tissue damage. The bone and muscle insertions were maintained to keep the physiologically relevant boundary conditions of the tendons and aid in sample handling for mechanical testing. Tendons were adhered directly to laser-cut PET frames at the bone and muscle insertions using Loctite Super Glue Gel Control (Fig. 2A; Supplemental Fig. 2H) and were immediately immersed in a large volume of PBS. Direct

contact between the tendons and glue was avoided to prevent altering the composition of the tendons. Samples were either stained immediately as follows or decellularized as described below. Tendons were rinsed in 1× PBS and stained with AF488-conjugated WGA (ThermoFisher) to visualize proteoglycans, diluted 1:50 in blocking buffer [10% donkey serum (Lampire) in 1× PBST] for 1 hr at room temperature.

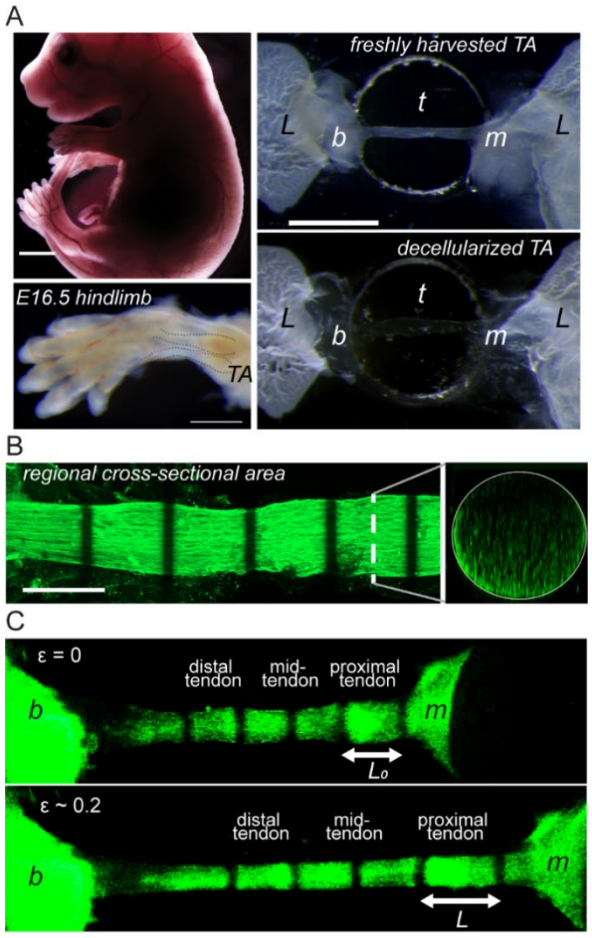

Figure 2. Isolation and preparation of E16.5 murine tendon for tensile testing. (A) The TA muscle – tendon – bone units were carefully dissected from freshly harvested embryos. To minimize damage to the tendon (*t*) during processing as well as to attach them to the 3D printed spring part during mechanical testing, muscle – tendon – bone units were glued onto PET frames using Loctite (*L*) at the muscle (*m*) and the bone (*b*) insertions (bars = 1 mm). (B) Tendons were stained with AF488-conjugated wheat germ agglutinin, and photobleached with a Zeiss 800 confocal to obtain fiducial lines for optically measuring strain. Full-thickness z-stacks were obtained to enable quantification of the cross-sectional area (bar = 200 μm). (C) Full field images of E16.5 decellularized TA tendon atε = 0.0 and 0.2 showing the regions investigated along the tendon.

Samples were mounted onto the springs and kept hydrated with PBS at all times. Fiducial lines were photobleached and cross-sectional areas were calculated, as described above (Fig. 2B). E16.5 tendons were tested using 4 mm × 6 mm frames and spring 1 (n = 3), while E18.5 tendons were tested using 4 mm × 7.65 mm frames and spring 2 (n = 3) (Supplemental Fig. 1C). Tensile tests to failure were conducted at 0.01 s^{-1} strain rate without preconditioning. Stress-strain datapoints were fit to polynomial functions for the calculation of the tangent moduli at relevant strain values. Embryonic tendon data sets were fit to a second order polynomial with the y-intercept set at the origin.

1.4.6. Decellularization of tendons

E16.5 and E18.5 TA muscle-tendon-bone units, secured to PET frames, were incubated in 8 mL 0.05% sodium dodecyl sulfate (SDS) with 1× Halt protease inhibitor (PI, ThermoFisher) in 1× PBS and gently rocked overnight. Completion of decellularization was determined by subjective visual inspection of samples and when ECM visualization was enhanced after immunostaining[49,50]. Upon decellularization, samples were rinsed in an excess of 1× PBS for 1 hr and stained and imaged prior to mechanical testing as described above. Tensile tests were conducted at 0.01 s^{-1} strain rate and loading by prescribing either a 5,000 μm displacement, a displacement equivalent to 100% strain based on actuator displacement, or until material failure. Samples were hydrated with PBS at all stages of testing. The regional stress-strain response corresponding to an individual pair of lines was averaged along the entire sample to investigate the effect of decellularization on E16.5 tendons and compare the mechanics of decellularized E16.5 (n = 3) and E18.5 (n = 3) embryonic timepoints (Fig. 2C). The purpose of testing decellularized tendons is twofold: to isolate and study the contribution of the ECM in the

mechanics of embryonic tendons and investigate if our system could resolve differences in mechanical properties as a function of treatment (i.e., decellularization) by testing both untreated and treated tendons.

1.5.Statistical methods

All the statistical analyses were conducted using GraphPad Prism 8.4.2 (GraphPad Software). A two-way ANOVA and Tukey's post hoc test were performed to evaluate differences in the mean tangent moduli between Solaris samples tested with different instruments (i.e., custom FemtoTools system and TA.XT*Plus* Connect). To evaluate tendon mechanics as a function of decellularization, residuals were checked for normality and Gaussian distribution. Residuals did not pass Shapiro-Wilk and D'Agostino-Pearson omnibus tests, so a two-way ANOVA was performed on the $\log_{10}$ of the tangent moduli. For the evaluation of tendon mechanics as a function of development, a two-way ANOVA with Sidak multiple comparisons was conducted on the mean tangent moduli at each stage. For the evaluation of regional stiffness in E16.5 tendons, a two-way ANOVA and Tukey's post hoc test was performed.

2. Results

2.1.Spring Design

A commercially available FemtoTools micromanipulator system was adapted to enable the optical measurement of strain while keeping biological samples hydrated in a bath. To mitigate the risk of damaging the microforce sensing probe with the PBS used to keep samples hydrated, 3D printed springs were designed. Three different springs were designed to accommodate various sample geometries (Supplemental Fig. 1). Custom PET frames for each spring were laser cut and used to secure the samples while processing and mounting onto the spring. The coil design for

springs 1-3 was the same; however, the spacing between the frame attachment sites were modified to accommodate the geometry of the different frames and biological samples. The spacing between the fixed and moveable sections of the spring were 2 mm, 3.7 mm, and 8.5 mm for spring 1, spring 2, and spring 3, respectively.

The spring and sample are loaded in parallel (Fig. 1D). Forces in parallel are additive, i.e., $F_{combined} = F_{spring} + F_{sample}$. Therefore, the force contribution from the spring alone (baseline) was subtracted to isolate the force contribution from the sample ($F_{sample} = F_{combined} - F_{spring}$; Fig. 1F). The force necessary to deform the three different spring designs was comparable; the force responses (tangent of the loading curve at a 250 μm displacement) of spring 1, spring 2, and spring 3 for a 1000 μm displacement at 10μm/s were 0.61 μN/μm, 0.67 μN/μm, and 0.62 μN/μm, respectively (Supplemental Fig. 4A). The stiffness of the spring was higher immediately after 3D printing and post-processing, with an initial force response (tangent of the loading curve at a 250 μm displacement) of 2.84 μN/μm. However, as the spring was loaded and unloaded over time, the stiffness decreased and reached a stable force response (Supplemental Fig. 4B). From days 0 – 7, there was a cumulative loading displacement of 2.1 mm, and the force response of spring 1 ranged from 2.88 μN/μm to 0.58 μN/μm, the average and standard deviation were 1.72 ± 0.96 μN/μm. From weeks 5 – 21, there was a cumulative loading displacement of 275.0 mm, and the force response of spring 1 ranged from 0.61 μN/μm to 0.41 μN/μm, the average and standard deviation were 0.51 ± 0.09 μN/μm. The trend in decreasing standard deviation as spring 1 was loaded and unloaded over time, suggests that the spring will reach a fatigue limit with use and settle to a constant force response. The variation in the initial stiffness of the spring serves to highlight the importance of why the baseline contribution was measured prior to testing samples to account for the force contribution from the springs.

Adding PBS to the liquid-retention basin led to a predictable effect on the mechanical response of the spring. The stiffness of the spring was higher when it was dry than when it was immersed in PBS. The initial stiffness (tangent at 250 μm displacement), from two measurements taken 7 minutes apart, was 2.34 ± 0.02 μN/μm. After the spring was exposed to PBS for approximately 90 minutes, the stiffness decreased to 0.66 ± 0.01 μN/μm, whereas 16.3 hours (994 minutes) later, the stiffness remained unchanged 0.64 ± 0.02 μN/μm (Supplemental Fig. 5). Therefore, the spring should be placed in PBS at least 90 minutes prior to mechanical testing to achieve a stable baseline. Once a baseline force response was established, the force response of the spring did not significantly change before and after sample testing ($p = 0.32$, Student's t-test). The pre-test baseline stiffness of the spring (tangent at 250 μm displacement) was 0.61 ± 0.02 μN/μm ($n = 3$). Post-test baselines were recorded after testing fibrin gel samples and the spring stiffness was 0.58 ± 0.05 μN/μm ($n = 3$; Supplemental Fig. 6).

2.2. Validation of spring-micromanipulator system

To confirm that the system could accurately determine the stress-strain response of a material of known properties, Solaris, a platinum-cure silicone rubber, was tested using both our system and a commercially available tensile-tester, TA.XT*Plus* Connect. Furthermore, two different spring configurations, spring 1 and spring 2, which have the same spring geometry, but were designed to test materials of different lengths, were compared to investigate if variations in design influenced the characterization of the material properties. Representative curves from the three configurations qualitatively showed similar stress-strain responses (Fig. 3A); however, the slope was larger by 29% at $\varepsilon = 0.1$ for samples tested with the TA.XT*Plus* instrument. Quantification of the tangent moduli showed no significant difference between the two spring

configurations, while the stress-strain response of the bulk material diverged from these values at lower strains (Fig. 3A).

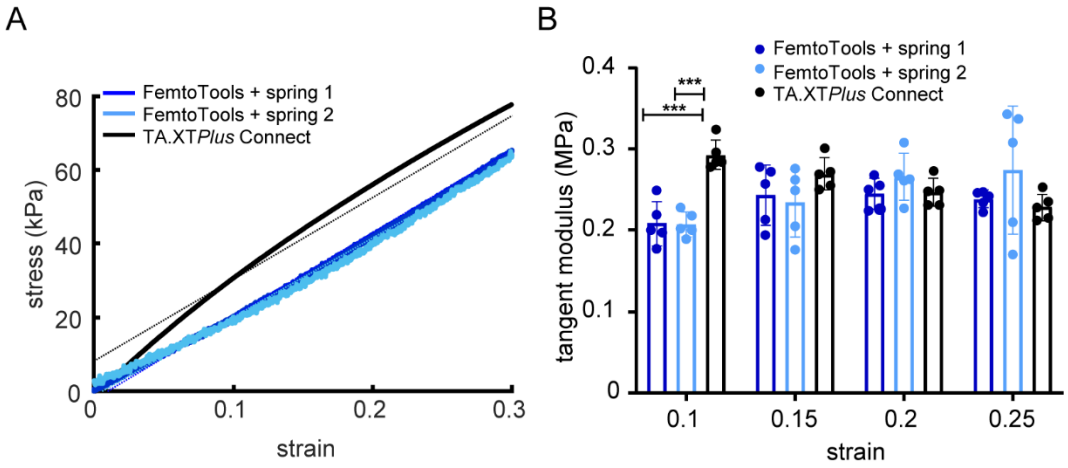

Figure 3. Validation of FemtoTools micromanipulator system. Solaris silicone samples were tested using our FemtoTools system with two different spring configurations and a TA.XT*Plus* Connect bulk material testing instrument. (A) Representative stress-strain curves of Solaris samples on the two instruments. The dotted line is a linear curve fitting of the Solaris sample tested on the TA.XT*Plus* Connect. (B) Comparison of the tangent moduli of Solaris tested on the FemtoTools system and TA.XT*Plus* Connect (FemtoTools + spring 1 (n=5), FemtoTools + spring 2 (n=5), TA.XT*Plus* Connect (n=5); error bars = std. dev.; two-way ANOVA, followed by Tukey's post hoc test: ***p<0.0002, ****p<0.0001).

This divergence was indicated at ε = 0.1, where the tangent moduli of Solaris samples tested with FemtoTools (spring 1: 0.208 ± 0.024 MPa; spring 2: 0.207 ± 0.014 MPa) were significantly different than those tested with the TA.XT*Plus* system (0.293 ± 0.016 MPa) (Fig. 3B). Testing Solaris on spring 1 and spring 2 with the FemtoTools system did not lead to significantly different tangent moduli for this material. At strain values of 0.15 (FemtoTools spring 1: 0.243 ± 0.033 MPa; FemtoTools spring 2: 0.234 ± 0.037 MPa; TA.XT*Plus*: 0.269 ± 0.018 MPa), 0.2 (FemtoTools spring 1: 0.245 ± 0.017 MPa; FemtoTools spring 2: 0.266 ± 0.026 MPa; TA.XT*Plus*: 0.246 ± 0.015 MPa), and 0.25 (FemtoTools spring 1: 0.238 ± 0.009 MPa; FemtoTools spring 2: 0.274 ± 0.070 MPa; TA.XT*Plus*: 0.229 ± 0.015 MPa) there were no significant differences in the tangent moduli obtained for Solaris with all 3 different testing configurations.

Using the FemtoTools system with both spring 1 and spring 2, yielded comparable results to the tangent moduli of Solaris measured by the *TA.XTPlus* tensile tester. There were no statistical differences between the tangent moduli of Solaris measured by spring 1 and spring 2. This validation verifies the capability of the system to accurately characterize mechanical properties.

2.3. Uniaxial loading of various materials

The versatility of the system was demonstrated by uniaxially testing a variety of soft materials, specifically fibrin gels, sheets of fibrillar fibronectin, and embryonic murine TA tendons. The force-displacement response of these disparate samples can be clearly resolved after subtracting the baseline contribution of the spring (Fig. 4).

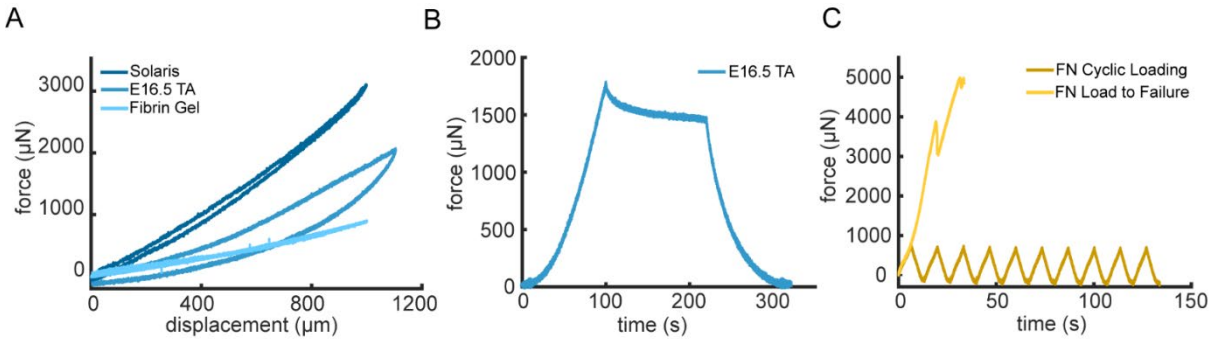

Figure 4. Resolution of the mechanics of soft tissues and biomaterials in response to a variety of tests. Baseline-adjusted curves. (A) Tensile loading and unloading curves of Solaris, E16.5 TA tendon, and fibrin gel. At a 1000 μm displacement during loading, the baseline adjusted force values for Solaris, E16.5 TA tendon, and fibrin gel were 3110 μN, 1786 μN, and 899 μN, respectively. At 1000 μm displacement, the raw force values of Solaris, E16.5 tendon, and fibrin gel were 407%, 282%, 155% greater than their respective baselines at the same displacement values. (B) Stress relaxation test for E16.5 TA tendon. (C) Cyclic loading and tensile loading to failure for fibronectin (FN) sheet. At 16.7 seconds (equivalent to 1000 μm displacement), the baseline adjusted force value for fibronectin was 3256 μN, this was 292% greater than the respective baseline force value at the same time.

At a 1000 μm displacement during loading, the baseline adjusted force values for Solaris, E16.5 TA tendon, and fibrin gel were 3110 μN, 1786 μN, and 899 μN, respectively. At 1000 μm displacement, the raw force values of Solaris, E16.5 tendon, and fibrin gel were 407%, 282%, 155%

greater than their respective baselines at the same displacement values. At 16.7 seconds (equivalent to 1000 μm displacement), the baseline adjusted force value for the fibronectin sheet was 3256 μN, this was 292% greater than the respective baseline force value at the same time. Additionally, our system was able to perform a variety of mechanical tests and measure different mechanical responses. For instance, Solaris and E16.5 TA tendon displayed viscoelastic properties, as observed by the hysteresis in tensile test (Fig. 4A) and stress relaxation curves (Fig. 4B). In contrast, the fibrin gel was elastic (Fig. 4A). The fibronectin sheet demonstrated the ability of the system to perform cyclic loading and loading to failure (Fig. 4C). We previously showed that the average tangent modulus of these fibronectin sheets was 0.63 ± 0.34 MPa at ε=0.25[23] which is comparable to moduli reported in literature 0.1 – 3.5 MPa[51]. Conversion of the force-displacement curves of 2 mg/mL fibrin gels to stress and strain found the average tangent modulus at ε=0.25 was 0.15 ± 0.08 MPa, which is comparable to moduli reported in literature for individual fibrin fibrils 1.7 ± 1.3 MPa[21,51].

2.4.Stress-strain evaluation of embryonic murine tendon ECM

To demonstrate that our system can resolve differences in mechanics of small, soft tissues as a function of developmental stage, we investigated how embryonic tendon mechanics vary due to development and cellularity. The regional stress-strain response (i.e., corresponding to an individual pair of photobleached lines) was averaged along the entire sample to compare E16.5 and E18.5 embryonic timepoints. The tangent moduli calculated at different strains for each sample were plotted for both developmental timepoints (Fig. 5A). To isolate the mechanical contribution of cells and the ECM of developing tendons, we decellularized tendons and compared the stress-strain response to freshly harvested tendons. The evaluation of E16.5 tendons showed decellularization had a significant effect on the tangent moduli according to a two-way ANOVA.

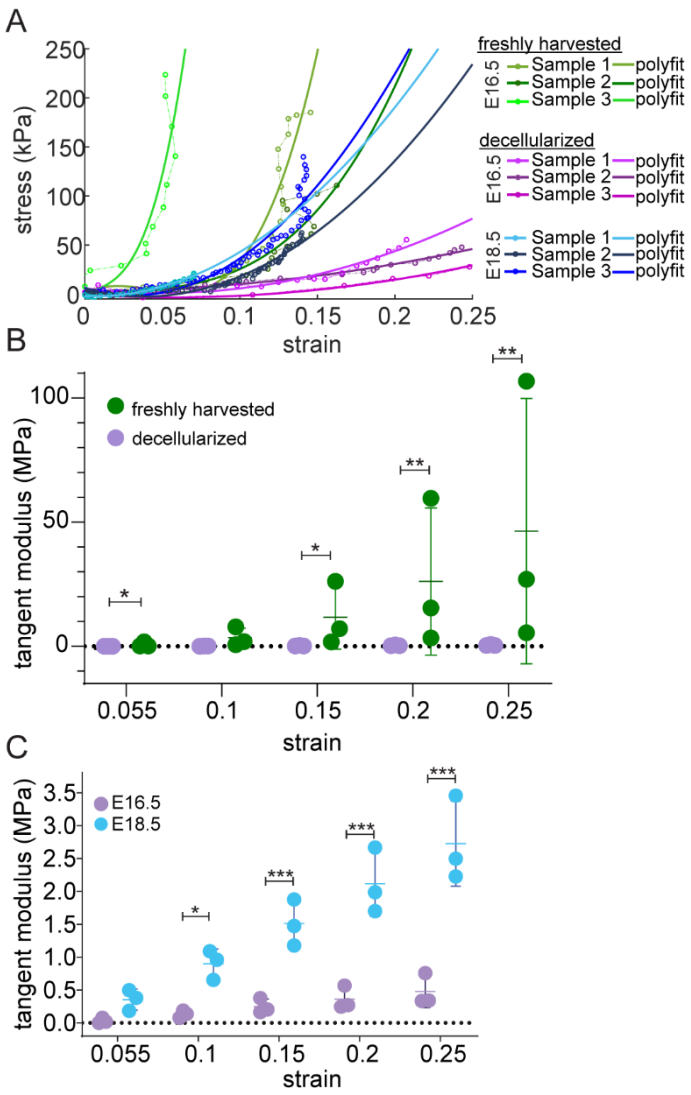

Figure 5. Mechanical behavior of embryonic tendons. (A) Stress-strain curves for freshly harvested E16.5 tendons (green), and decellularized E16.5 (purple) and E18.5 (blue) samples, along with the fitted polynomials. (B) Tangent moduli of freshly harvested and decellularized E16.5 tendons were significantly different. (Sidak multiple comparisons: *$0.0021 < p \leq 0.0332$; **$0.0002 < p \leq 0.0021$; n = 3; error bars = std. dev.) (C) The tangent moduli of decellularized tendons at E18.5 were significantly greater than those harvested at E16.5 for $\varepsilon \geq 0.1$. (Sidak multiple comparisons: *$0.0021 < p \leq 0.0332$; **$0.0002 < p \leq 0.0021$, ***$0.0002 < p \leq 0.0001$, **** $p < 0.0001$; n = 3; error bars = std. dev.)

Multiple comparisons showed significant differences between individual groups except at $\varepsilon = 0.1$, potentially due to the large variability in the dataset, the sample size, and the efficacy of the decellularization method to remove all cellular components (Fig. 5B). For instance, at $\varepsilon=0.05$

the average tangent moduli for freshly harvested E16.5 was 0.729 ± 0.803 MPa, whereas the average for decellularized E16.5 tendons was 0.033 ± 0.033 MPa, indicating high variability based on the standard deviation. Similarly, at ε=0.25 the average tangent moduli were 26.166 ± 24.178 MPa for the freshly harvested E16.5 tendons and 0.363 ± 0.145 MPa for the decellularized E16.5 samples. The evaluation of embryonic decellularized tendons with a two-way ANOVA showed a significant increase in moduli as a function of development. Multiple comparisons indicated significant differences in the tangent moduli between individual groups of E16.5 and E18.5 tendons at strain values greater than 0.1 (Fig. 5C).

Further, regional variability in tangent moduli was observed for E16.5 decellularized tendons. The stress-strain response indicated the stiffness of the tendon at the distal region was greater than the mid and proximal ends (Fig. 6A). Two-way ANOVA indicated both strain value and region along the tendon had a significant effect on the tangent moduli of E16.5 decellularized TA, indicating nonlinear behavior (Fig. 6B). Two strain values were then compared, actuator strain and optical strain. Actuator strain was calculated from the displacement imposed by the FemtoTools micromanipulator. Optical strain was calculated from the average distance between fiducial lines that were photobleached onto the sample from videos acquired during uniaxial tensile tests. The importance of using fiducial makers to evaluate strain for soft materials is highlighted by the differences between actuator and optical strain for E16.5 and E18.5 tendons and fibronectin sheets (Supplemental Fig. 7). For example, at ε=0.15 the tangent modulus based on optical strain (0.970 MPa) was more than 25-fold greater than that based on the actuator strain (0.038 MPa) for a freshly harvested E16.5 tendon.

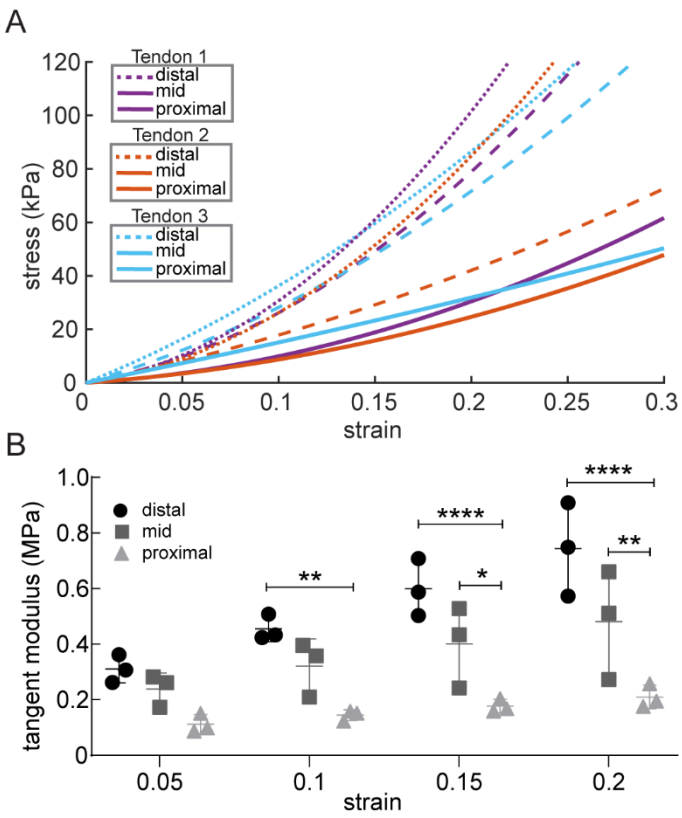

Figure 6. TA tendons show regional variability at E16.5. (A) Polynomial fits of the stress-strain response of decellularized E16.5 TA tendons at different regions. (B) Tukey multiple comparisons showed significant differences in the tangent moduli between individual groups (*$0.0021 < p \leq 0.032$; **$0.0002 < p \leq 0.0021$, ***$0.0002 < p \leq 0.0001$, **** $p < 0.0001$; n = 3; error bars = std. dev.)

3. Discussion

In this study, we designed a modular device capable of assessing the mechanical behavior of soft biomaterials and showcased the ability of the system to mechanically characterize embryonic tissues at different developmental timepoints. We customized a commercially available micromanipulator with a force resolution of 5 nN – 50 µN and a displacement sensing range starting at 5 nm, facilitating the application of displacements on small samples while recording force. The modularity and small footprint of the system allowed testing under a dissecting microscope to enable the calculation of optical strain (Fig. 1A). Our data demonstrate the capability of the FemtoTools micromanipulator and spring system to resolve the force of samples

by subtracting the contribution of the spring itself (Fig. 2A). The system was validated by mechanically characterizing Solaris, a reference material with known material properties (Fig. 2B,C). The spring design was modified to measure the tensile response of fibronectin sheets, fibrin gels, and embryonic tendons. The modularity of the system allowed us to test tissues of different stiffnesses and sizes and can be used to mechanically characterize soft biomaterials and small tissues to obtain physiologically relevant design parameters for scaffolding that seek to emulate native tissue mechanics.

When considering a testing system, the force resolution, maximum force capacity, and the gauge dimensions determine the tissues that can be tested with the system. Force and displacement curves showed minimal noise in unfiltered data (Fig. 4), eliminating the need for processing through filtering and noise-reducing algorithms. The appropriately sized 3D printed spring and microforce sensor with sufficiently high force threshold were selected according to the material size and estimated stiffness prior to tensile testing. When testing developing tissues that change in size and stiffness as a function of development, the adaptability of the system and the force resolution are critical. The force sensing capability of the FemtoTools microsensors is between 100 μN threshold with 5 nN resolution and 100,000 μN threshold with 50 μN resolution. A limitation of this system is measuring tissues that have resultant forces outside of this range during tensile testing, e.g., adult tibialis anterior tendons. Since there are commercially available tensile systems that operate outside of the FemtoTools force threshold, a combination of instruments may be necessary to fully characterize tissues across development. Adapting to different geometries was feasible given the ease of fabrication through 3D printing of springs and laser cutting of PET frames. The modularity of the system will enable future multiscale studies given that the micromanipulator system can be coupled with the microscope of choice (e.g., dissecting, confocal)

to investigate deformation at a range of scales. The ability to use the same instrument for tensile testing at different scales can facilitate meaningful studies relating the micro- and macroscales. While commercially available bioreactor systems such as the BioTense Perfusion Bioreactor System (Admet) include similar features (e.g., mounting on a microscope, bath, application of uniaxial force, actuator control), the focus on the cellular scale may lead to limitations with mechanically characterization at the tissue scale, especially with larger samples[52]. Further, for the *ex vivo* mechanical testing of decellularized or immunostained tissues, there is little need for bioreactor features such temperature control and maintaining concentration of nutrients through perfusion.

The results obtained for the elastomer Solaris were similar to those reported by others and by the manufacturer[43,53]. There was a discrepancy in the tangent moduli at $\varepsilon \leq 0.1$, where the bulk material testing system recorded a greater modulus. This is attributed to differences in the casting and curing protocols for samples generated for the FemtoTools and TA.XT*Plus* systems. Samples tested on the FemtoTools were fabricated via spin coating to generate a thin film of uniform thickness, potentially causing shear stress to align Solaris chains influencing the stress-strain response[54]. In contrast, the Solaris for bulk testing was polymerized in a mold and cured for longer at 70°C. Further, the samples tested with the FemtoTools systems were tested while surrounded by PBS, while those tested with the TA.XT*Plus* were surrounded by air during testing. Independent of fabrication differences, our instrument identified similar tangent moduli for Solaris tested with a bulk material tester. In addition, the material behavior observed for fibronectin sheets and fibrin gel are similar to those previously published, where the fibrin gels were linear elastic while fibronectin sheets were viscoelastic[55–57].The tangent modulus at $\varepsilon=0.25$ of fibronectin

sheets and fibrin gels measured by the FemtoTools system was comparable to moduli reported in literature for these materials[21,51].

Tendons are responsible for transferring the force produced by the muscle to the skeleton with high fidelity while avoiding musculoskeletal injury. Uniaxial tensile testing is most commonly used to characterize the bulk mechanical properties of adult tendon. Adult tendons are predominantly made up of ECM, whereas developing tendons have a substantially higher number of cells. In addition, embryonic tendons are much smaller, making it challenging to test using the standard instrumentation designed to handle larger, stiffer tissues. Given the challenges in isolating and testing embryonic murine tendons under tension, the mechanics of developing tendons are often studied using indentation modalities at the nano and microscales[16,17]; however, this is not the way in which tendons are typically loaded *in vivo*. The capabilities of our system enabled the characterization of embryonic murine tendon mechanics as a function of development based on uniaxial tensile loading and optical strain. As expected, tendons show viscoelastic behavior, as seen in the stress relaxation test and hysteresis when unloading (Fig. 4A,B). Tangent moduli calculated for E16.5 and E18.5 tendons significantly increased in stiffness as a function of development and varied regionally (Fig. 5A,C; Fig. 6), as previously demonstrated for rat and mouse tendons[27,42,58]. These data demonstrate our experimental and image processing methods can be reliably used to investigate the regional mechanics of small developing tissues.

The variability of tangent moduli among samples within a developmental timepoint could be due to biological variability. Further, the process of attaching tendons to PET frames could affect the mechanical behavior if glue was to cure onto the tendon surface. Future work will need to evaluate a larger sample sizes for each developmental timepoint to compensate for biological variability. This attachment mechanism will need to be further evaluated, since most of the samples

tested failed at the muscle insertion and slipping was often observed by dips in the force measurements recorded during testing[36]. This is attributed to a weak interface between the muscle surface and the glue. Slipping was one of the main factors that contributed to the differences between the actuator and optical strain (Supplemental Fig. 7). Future studies will investigate additional ways to secure the full thickness of the muscle tissue without compromising the integrity of the tendon, such as using a UV-curable glue that is more viscous or polymerizes more quickly in order to minimize the risk of the glue wicking onto the tendon surface while attaching the sample to the PET frame. Additionally, different attachment mechanisms that physically prevent the muscle surface from moving and slipping at the glue interface will be explored such as adding enclosures to the PET frames that facilitate completely immersing the muscle in an adhesive, rather than partially covering the muscle with adhesive. While gluing the tendon tissue directly to the frames may be more effective at minimizing slipping at the muscle interface, as is done in many studies, this involves removing the tendon from the native boundary conditions and shortens the overall gauge length, altering the material response during testing.

Notably, decellularization decreased the stiffness of embryonic tendons, as cells and intracellular proteins are removed. While cells are thought to minimally contribute to the mechanics of adult tendons, there was a significant decrease in the moduli of decellularized embryonic tendons (Fig. 5B). In addition, it appears that the regional variability is not due only to the cells but also the ECM as that is maintained after decellularization (Fig. 6). The residual cellular debris potentially present in the samples (e.g., DNA) could potentially contribute to the mechanical response of the decellularized tissues, and therefore future work would need to look at removing residual DNA to look at the ECM mechanical response in these tissues[59].

Although the mechanical contribution of the spring has been shown to not drastically change over time (Supplemental Fig. 4), it was still necessary to adjust for the spring contribution based on data collected the same day as mechanical testing to account for potential variations. After 360 tensile tests conducted over a 21-week period, we have not had to replace the spring due to material fatigue from cyclic testing. However, since we have not considered all potential testing conditions, we recommend regularly performing baseline tests of the spring, and discontinuing use if the baseline force-displacement response becomes irregular. The material properties of the springs are likely affected by polymer melting, resolution of 3D printing, and post-processing of each part. The tensile modulus of the 3D printed spring was orders of magnitude lower than that reported by the manufacturer[60]. This discrepancy needs further investigation to determine the effect of post-processing and printing orientation. Although the influence of aqueous solutions on the mechanical properties of the spring (Supplemental Fig. 5) was consistent and repeatable the mechanism by which PBS contributes to decreased spring stiffness will need to be further investigated. Future iterations of this system will utilize different materials such that the presence of PBS will not influence mechanical properties of the testing system.

4. Conclusions

These data show the ability of our system to characterize a variety of soft biomaterials and small tissues with different material properties. Mechanical characterization of tissues and ECM is vital for understanding the cellular microenvironment during growth and development. The small size and susceptibility to damage of embryonic tissues and soft biomaterials limit the use of tensile testing modalities typically used for adult soft tissues. This testing system can help better understand the mechanical properties of multifunctional ECM polymers, like fibrin and fibronectin, and the mechanical influence of these polymers during tissue growth and remodeling that are

currently not completely understood. By quantifying the material properties of soft biomaterials and small tissues, physiologically relevant parameters can be provided for the design and fabrication of regenerative therapies that aim to restore tissue functionality.

Acknowledgements

This work is supported by NIH R01 AR071359, NIH DP2 AT009833 and NSF CMMI 1911346 to S.C. The authors would like to thank Drs. Jacqueline Linnes and Elizabeth Phillips for assistance with laser cutting, Dr. David Umulis for the use of the Zeiss 800 upright confocal microscope, and Norvin Bruns for fabricating custom mounts and fixtures.

Supplementary Material (Appendix A)

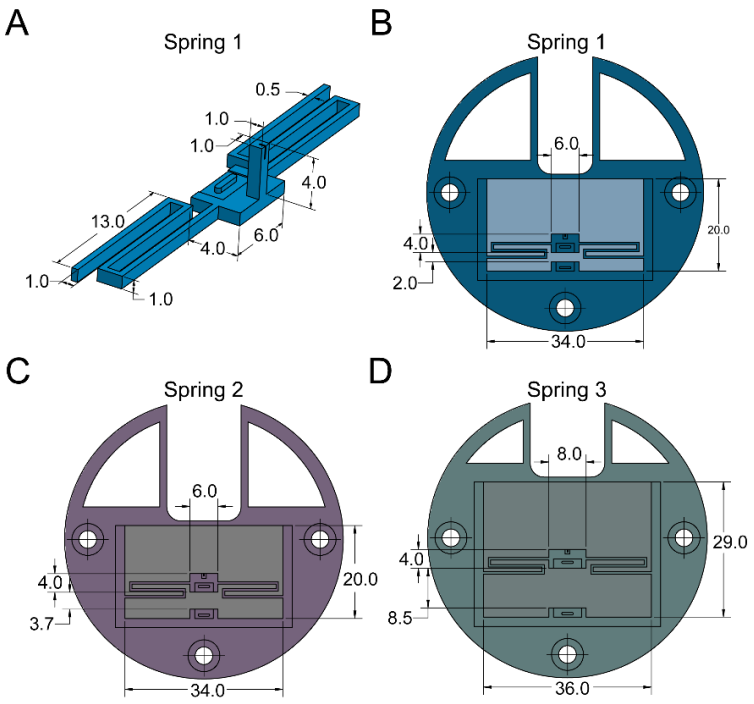

Supplemental Figure 1. **Spring designs to accommodate samples of different sizes.** (A) Spring 1 dimensions, isometric view. (B) Spring 1 dimensions, top view - 2.0mm gap between fixed and moveable frame anchor points. Used to test silicone and E16.5 murine TA tendons. (C) Spring 2 dimensions, top view - 3.7mm gap between fixed and moveable frame anchor points. Used to test silicone and E18.5 murine TA tendons. (D) Spring 3 dimensions, top view - 8.5mm gap between fixed and moveable frame anchor points. Used to test fibrin gel and fibronectin sheets. All dimensions in mm.

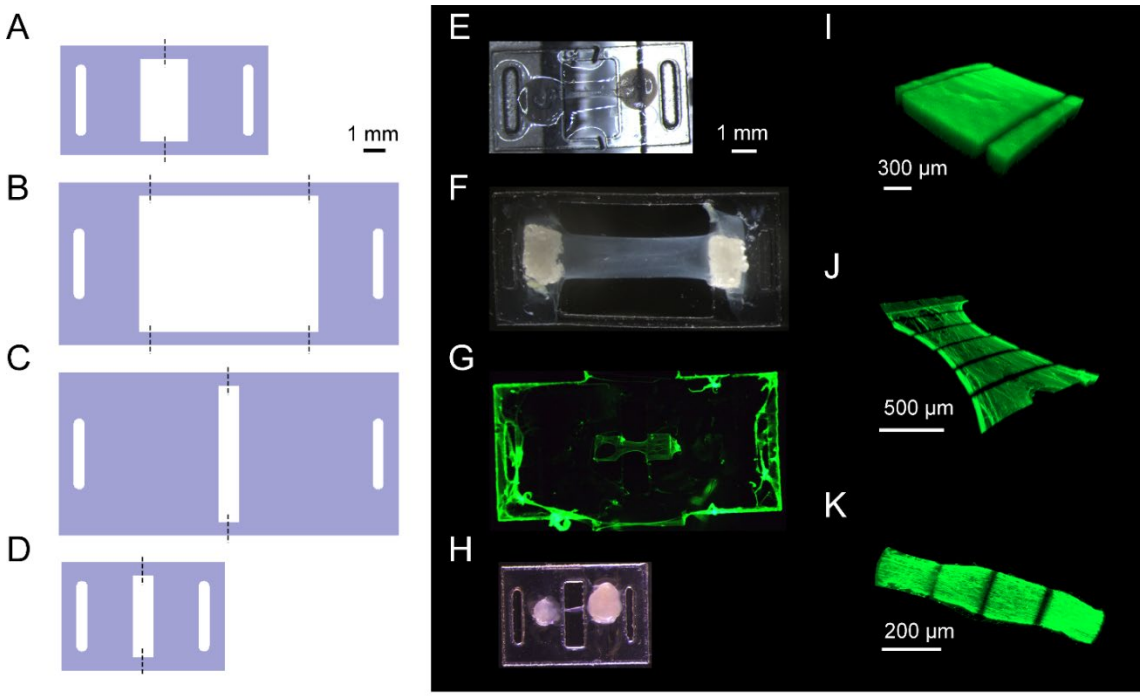

Supplemental Figure 2. **Frames mounted with various biomaterials**. Polyethylene terephthalate (PET) frames were laser cut to accommodate different sized materials: 4 mm × 7.65 mm frame with 1.65 mm wide window (A); 6 mm × 12.5 mm frame with 6.6 mm window (B); 6 mm × 12.5 mm frame with 1 mm window (C); 4 mm × 6 mm frame with 1 mm window (D). The dashed lines (A-D) indicate sites where frames were manually cut after sample was mounted to allow deformation during tensile testing. Images of biomaterials after mounting on PET frames: Solaris Silicone (E); fibrin gel (F); fibronectin sheet (G); E16.5 TA muscle – tendon – bone unit (H). Three-dimensional isometric views of z-stacks of fibrin gel (I); fibronectin sheet (J); E16.5 tendon (K). Scale bar for A – H = 1mm.

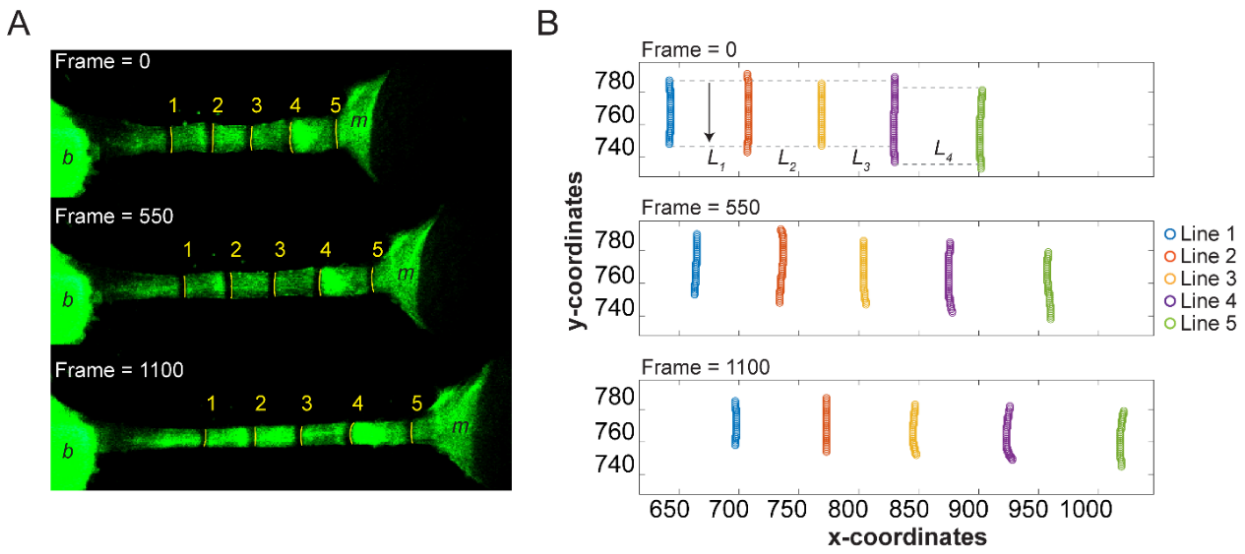

Supplemental Figure 3. **Optical measurement of displacement.** (A) A FIJI macro was used to manually trace the fiducial lines from frames of the recorded videos, and the *x* and *y* coordinates of each manually drawn line were returned. Manually drawn Lines 1-5 displayed in yellow. (B) A MATLAB algorithm was used to measure the average horizontal distance between fiducial lines for each selected frame. The *x* and *y* coordinates of Lines 1-5 are displayed. Colors are assigned to each line to facilitate comparing the position of each line in different frames from the recorded video. Horizontal alignment between lines is denoted by the dashed lines on Frame 0. L_n (e.g. L_1) refers to the average horizontal distance between Line *n* and Line *n+1* (e.g. Line 1 and Line 2). Strain was calculated relative to the initial distance between fiducial lines.

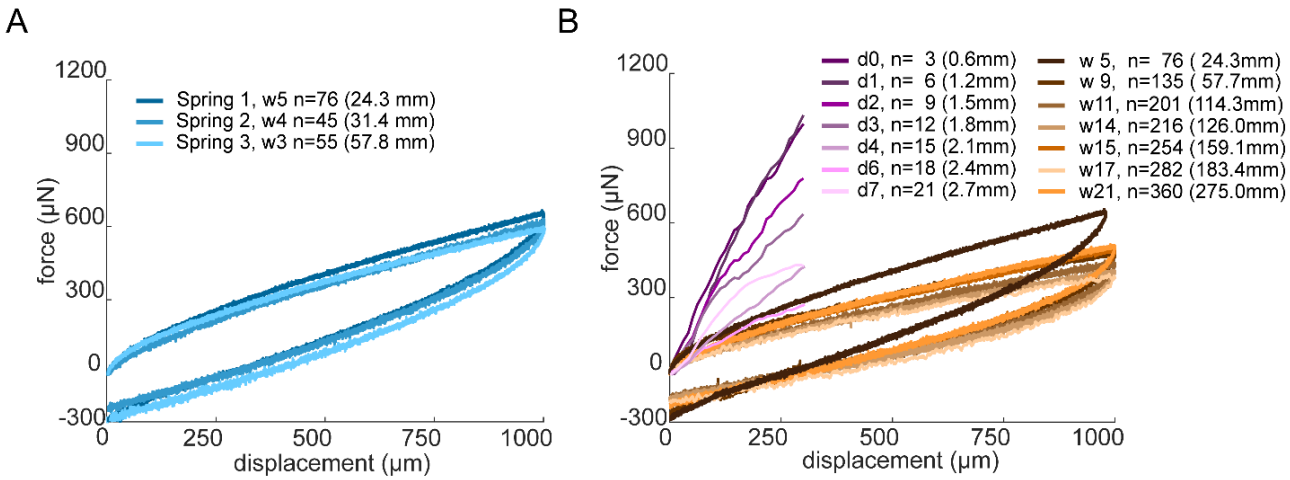

Supplemental Figure 4. Comparison of baseline response of 3D printed springs. (A) Force-displacement profiles for spring 1, spring 2, spring 3. The number of weeks (w) after printing and processing, number of loading/unloading cycles (n), and cumulative loading displacement are shown for reference. The tangent at a displacement of 250 µm the loading portion of the force response of spring 1, spring 2, and spring 3 have slopes of 0.62 µN/µm, 0.67 µN/µm, and 0.61 µN/µm, respectively. (B) Time study using spring 1 design. Short-term study was carried out at days (d) 0-7 after printing and post processing. Long-term study carried out between weeks (w) 5 – 21 after printing and post processing. Day 0-7 tests were run prior to optimizing acquisition parameters. The range in the force response (tangent at 250 µm displacement during loading) from d0 – d7 was from 2.88 µN/µm to 0.58 µN/µm, the average and standard deviation were 1.72 ± 0.96 µN/µm. The range in the force response from w5 – w21 was from 0.61 µN/µm to 0.41 µN/µm, the average and standard deviation were 0.51 ± 0.09 µN/µm.

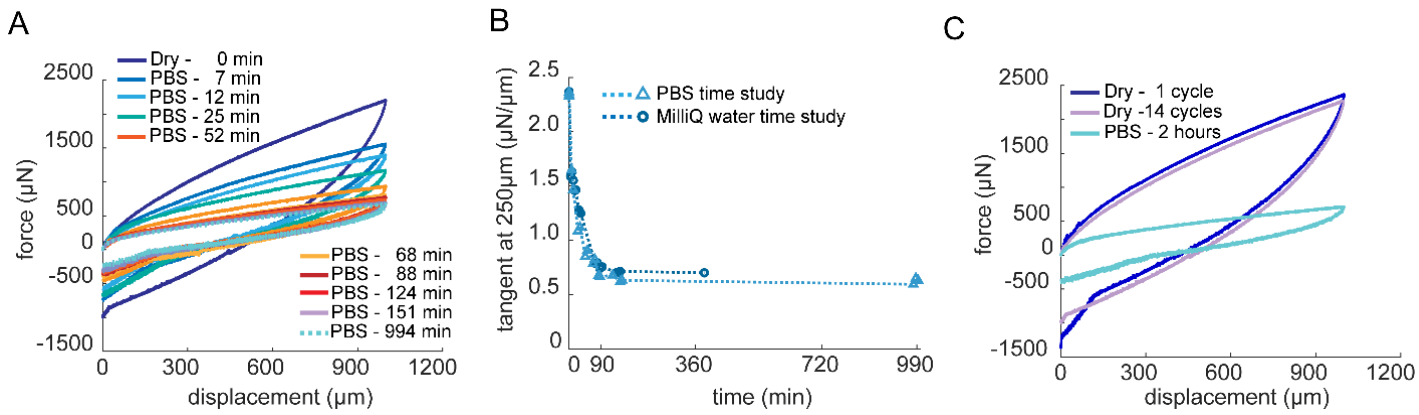

Supplemental Figure 5. Effect of aqueous solutions on the mechanical properties of 3D printed springs. (A) Representative force-displacement curves of spring 3 when dry, and 7, 12, 25, 52, 68, 124, 151 and 994 minutes after PBS was added to the liquid-retention basin. (B) The stiffness of the spring decreased when immersed in either PBS or MilliQ water. The stiffness (tangent at 250 µm displacement) decreased from 2.34 ± 0.02 µN/µm (n = 3) when dry to 0.66 ± 0.01 µN/µm (n = 2) after 90 min in PBS and remained at 0.64 ± 0.02 µN/µm (n = 2) after 16.3 hours (994 minutes). (C) Representative force-displacement curves of the dry spring after removal of PBS. The first loading cycle demonstrated the recovery of the spring after drying (stiffness = 2.37 µN/µm at 250 µm). After 14 loading and unloading cycles, the stiffness was not substantially changed (2.51 µN/µm). The spring was then incubated in PBS for 2 hours without additional loading cycles, and the stiffness decreased to 0.62 µN/µm. These data indicate the results in A and B were due to equilibration in aqueous solutions rather than softening due to repeated loading.

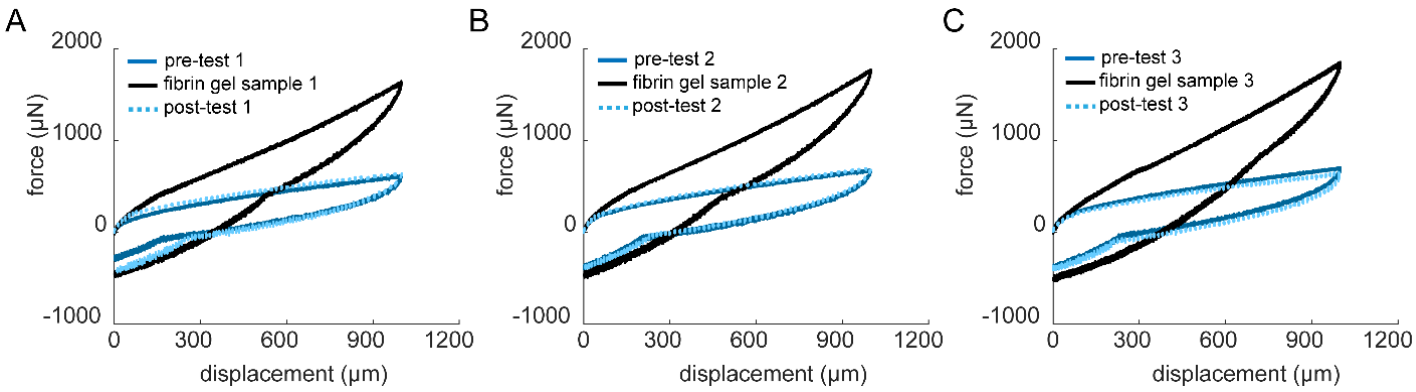

Supplemental Figure 6. Baseline response of spring 3 pre- and post-test. (A-C) Three different 2 mg/mL fibrin gels were tested and the force-displacement curves of the spring were recorded before and after. The stiffness of the springs was measured at 250 μm during loading portion. There was no significant difference in the stiffness pre- and post-test: 0.61 ± 0.02 μN/μm and 0.58 ± 0.05 μN/μm, respectively (n = 3; p = 0.32, Student's t-test).

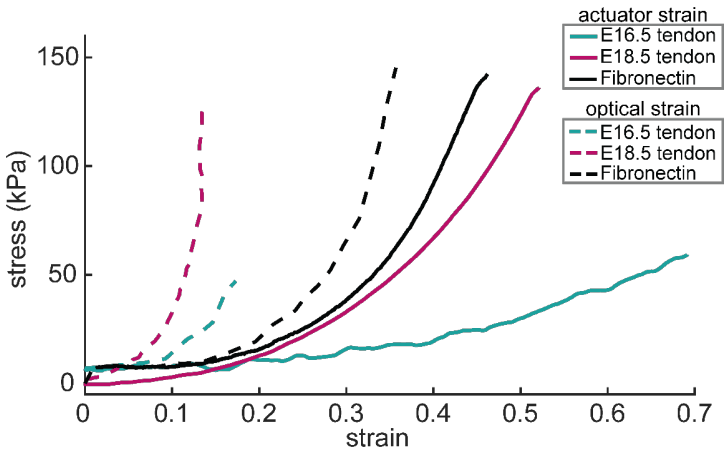

Supplemental Figure 7. Actuator and optical strain comparison. The discrepancy between actuator strain and optical strain for representative E16.5 tendon, E18.5 tendon, and fibronectin samples, highlights the importance of using optical strain to more accurately represent the deformation as measured directly from the sample, rather than the sample attachment points.

References (Appendix A)

[1] J.K. Mouw, G. Ou, V.M. Weaver, Extracellular matrix assembly: a multiscale deconstruction, Nat. Publ. Gr. 15 (2014). https://doi.org/10.1038/nrm3902.

[2] N.D. Murchison, B.A. Price, D.A. Conner, D.R. Keene, E.N. Olson, C.J. Tabin, R. Schweitzer, Regulation of tendon differentiation by scleraxis distinguishes force-transmitting tendons from muscle-anchoring tendons, Development. 134 (2007) 2697–2708. https://doi.org/10.1242/dev.001933.

[3] C.C. Banos, A.H. Thomas, C.K. Kuo, Collagen fibrillogenesis in tendon development: Current models and regulation of fibril assembly, Birth Defects Res. Part C - Embryo Today Rev. 84 (2008) 228–244. https://doi.org/10.1002/bdrc.20130.

[4] K.C. Clause, T.H. Barker, Extracellular matrix signaling in morphogenesis and repair, Curr. Opin. Biotechnol. 24 (2013) 830–833. https://doi.org/10.1016/j.copbio.2013.04.011.

[5] D.E. Discher, P. Janmey, Y.L. Wang, Tissue cells feel and respond to the stiffness of their substrate, Science (80-.). 310 (2005) 1139–1143. https://doi.org/10.1126/science.1116995.

[6] C. Bonnans, J. Chou, Z. Werb, Remodelling the extracellular matrix in development and disease, Nat. Rev. Mol. Cell Biol. 15 (2014) 786–801. https://doi.org/10.1038/nrm3904.

[7] M.W. Pickup, J.K. Mouw, V.M. Weaver, The extracellular matrix modulates the hallmarks of cancer, EMBO Rep. 15 (2014) 1243–1253. https://doi.org/10.15252/embr.201439246.

[8] D.E. Birk, E.I. Zycband, S. Woodruff, D.A. Winkelmann, R.L. Trelstad, Collagen fibrillogenesis in situ: Fibril segments become long fibrils as the developing tendon matures, Dev. Dyn. 208 (1997) 291–298. https://doi.org/10.1002/(SICI)1097-0177(199703)208:3<291::AID-AJA1>3.0.CO;2-D.

[9] H.L. Ansorge, S. Adams, D.E. Birk, L.J. Soslowsky, Mechanical, Compositional, and Structural Properties of the Post-natal Mouse Achilles Tendon, (2011). https://doi.org/10.1007/s10439-011-0299-0.

[10] N.R. Schiele, J.E. Marturano, C.K. Kuo, Mechanical factors in embryonic tendon development: Potential cues for stem cell tenogenesis, Curr. Opin. Biotechnol. 24 (2013) 834–840. https://doi.org/10.1016/j.copbio.2013.07.003.

[11] W.P. Daley, S.B. Peters, M. Larsen, Extracellular matrix dynamics in development and regenerative medicine, (n.d.). https://doi.org/10.1242/jcs.006064.

[12] B.K. Connizzo, S.M. Yannascoli, L.J. Soslowsky, Structure–function relationships of postnatal tendon development: A parallel to healing, Matrix Biol. 32 (2013) 106–116. https://doi.org/10.1016/J.MATBIO.2013.01.007.

[13] A.R. Ocken, M.M. Ku, T.L. Kinzer-Ursem, S. Calve, Perlecan knockdown significantly alters extracellular matrix composition and organization during cartilage development, Mol. Cell. Proteomics. (2020) mcp.RA120.001998. https://doi.org/10.1074/mcp.ra120.001998.

[14] J.E. Wagenseil, C.H. Ciliberto, R.H. Knutsen, M.A. Levy, A. Kovacs, R.P. Mecham, Reduced Vessel Elasticity Alters Cardiovascular Structure and Function in Newborn Mice, (n.d.). https://doi.org/10.1161/CIRCRESAHA.108.192054.

[15] L. Carta, L. Pereira, E. Arteaga-Solis, S.Y. Lee-Arteaga, B. Lenart, B. Starcher, C.A. Merkel, M. Sukoyan, A. Kerkis, N. Hazeki, D.R. Keene, L.Y. Sakai, F. Ramirez, Fibrillins 1 and 2 perform partially overlapping functions during aortic development, J. Biol. Chem. 281 (2006) 8016–8023. https://doi.org/10.1074/jbc.M511599200.

[16] J.E. Marturano, J.D. Arena, Z.A. Schiller, I. Georgakoudi, C.K. Kuo, Characterization of mechanical and biochemical properties of developing embryonic tendon, Proc Natl Acad Sci USA. 110 (2013) 6370–6375. https://doi.org/10.1073/pnas.1300135110.

[17] X.S. Pan, J. Li, E.B. Brown, C.K. Kuo, Embryo movements regulate tendon mechanical property development., Philos. Trans. R. Soc. Lond. B. Biol. Sci. 373 (2018) 20170325. https://doi.org/10.1098/rstb.2017.0325.

[18] N.S. Kalson, D.F. Holmes, A. Herchenhan, Y. Lu, T. Starborg, K.E. Kadler, Slow stretching that mimics embryonic growth rate stimulates structural and mechanical development of tendon-like tissue in vitro, Dev. Dyn. 240 (2011) 2520–2528. https://doi.org/10.1002/dvdy.22760.

[19] A. Subramanian, T.F. Schilling, Tendon development and musculoskeletal assembly: emerging roles for the extracellular matrix, (2015). https://doi.org/10.1242/dev.114777.

[20] C.J. Miller, L. a Davidson, The interplay between cell signalling and mechanics in developmental processes, Nat. Rev. Genet. 14 (2013) 733–744. https://doi.org/10.1038/nrg3513.

[21] P.A. Janmey, J.P. Winer, J.W. Weisel, Fibrin gels and their clinical and bioengineering applications, J. R. Soc. Interface. 6 (2009) 1–10. https://doi.org/10.1098/rsif.2008.0327.

[22] R. Pankov, K.M. Yamada, Fibronectin at a glance, J. Cell Sci. 115 (2002) 3861–3863. https://doi.org/10.1242/jcs.00059.

[23] Á. Enríquez, S. Libring, T.C. Field, J. Jimenez, T. Lee, H. Park, D. Satoski, M.K. Wendt, S. Calve, A.B. Tepole, L. Solorio, H. Lee, High-Throughput Magnetic Actuation Platform for Evaluating the Effect of Mechanical Force on 3D Tumor Microenvironment, Adv. Funct. Mater. (2020) 2005021. https://doi.org/10.1002/adfm.202005021.

[24] J.H. Jordahl, L. Solorio, H. Sun, S. Ramcharan, C.B. Teeple, H.R. Haley, K.J. Lee, T.W. Eyster, G.D. Luker, P.H. Krebsbach, J. Lahann, 3D Jet Writing: Functional Microtissues Based on Tessellated Scaffold Architectures, Adv. Mater. 30 (2018) 1707196. https://doi.org/10.1002/adma.201707196.

[25] Z.A. Glass, N.R. Schiele, C.K. Kuo, Informing tendon tissue engineering with embryonic development, J. Biomech. 47 (2014) 1964–1968. https://doi.org/10.1016/J.JBIOMECH.2013.12.039.

[26] N.R. Schiele, J.E. Marturano, C.K. Kuo, Mechanical factors in embryonic tendon development: Potential cues for stem cell tenogenesis, Curr. Opin. Biotechnol. 24 (2013) 834–840. https://doi.org/10.1016/j.copbio.2013.07.003.

[27] S. Calve, I.F. Lytle, K. Grosh, D.L. Brown, E.M. Arruda, Implantation increases tensile strength and collagen content of self-assembled tendon constructs, J Appl Physiol. 108 (2010) 875–881. https://doi.org/10.1152/japplphysiol.00921.2009.-Tissue-en.

[28] J.M. Silva Garcia, A. Panitch, S. Calve, Functionalization of hyaluronic acid hydrogels with ECM-derived peptides to control myoblast behavior, Acta Biomater. 84 (2019) 169–179. https://doi.org/10.1016/j.actbio.2018.11.030.

[29] A. Jorge-Peñas, H. Bové, K. Sanen, M.M. Vaeyens, C. Steuwe, M. Roeffaers, M. Ameloot, H. Van Oosterwyck, 3D full-field quantification of cell-induced large deformations in fibrillar biomaterials by combining non-rigid image registration with label-free second harmonic generation, Biomaterials. 136 (2017) 86–97. https://doi.org/10.1016/j.biomaterials.2017.05.015.

[30] X. Xu, Z. Li, L. Cai, S. Calve, C.P. Neu, Mapping the Nonreciprocal Micromechanics of Individual Cells and the Surrounding Matrix Within Living Tissues, Nat. Publ. Gr. (2016). https://doi.org/10.1038/srep24272.

[31] A.D. Doyle, K.M. Yamada, Mechanosensing via cell-matrix adhesions in 3D microenvironments, Exp. Cell Res. 343 (2016) 60–66. https://doi.org/10.1016/J.YEXCR.2015.10.033.

[32] M. Elhebeary, M.A.B. Emon, O. Aydin, M.T.A. Saif, A novel technique for in situ uniaxial tests of self-assembled soft biomaterials, Lab Chip. 19 (2019) 1153–1161. https://doi.org/10.1039/c8lc01273c.

[33] R.B. Svensson, S.T. Smith, P.J. Moyer, S.P. Magnusson, Effects of maturation and advanced glycation on tensile mechanics of collagen fibrils from rat tail and Achilles tendons, Acta Biomater. (2018). https://doi.org/10.1016/j.actbio.2018.02.005.

[34] C. Jayyosi, N. Lee, A. Willcockson, S. Nallasamy, M. Mahendroo, K. Myers, The mechanical response of the mouse cervix to tensile cyclic loading in term and preterm pregnancy, Acta Biomater. 78 (2018) 308–319. https://doi.org/10.1016/j.actbio.2018.07.017.

[35] X. Ye, Z. Cui, H. Fang, X. Li, A Multiscale Material Testing System for In Situ Optical and Electron Microscopes and Its Application, Sensors. 17 (2017). https://doi.org/10.3390/s17081800.

[36] M. Jiang, Z.T. Lawson, V. Erel, S. Pervere, T. Nan, A.B. Robbins, A.D. Feed, M.R. Moreno, Clamping soft biologic tissues for uniaxial tensile testing: A brief survey of current methods and development of a novel clamping mechanism, J. Mech. Behav. Biomed. Mater. 103 (2020) 103503. https://doi.org/10.1016/j.jmbbm.2019.103503.

[37] H.B. Henninger, B.J. Ellis, S.A. Scott, J.A. Weiss, Contributions of elastic fibers, collagen, and extracellular matrix to the multiaxial mechanics of ligament, J. Mech. Behav. Biomed. Mater. (2019). https://doi.org/10.1016/j.jmbbm.2019.07.018.

[38] J.D. Humphrey, D.L. Vawter, R.P. Vito, Quantification of strains in biaxially tested soft tissues, J. Biomech. 20 (1987) 59–65. https://doi.org/10.1016/0021-9290(87)90267-3.

[39] M.J. Bradshaw, G.A. Hoffmann, J.Y. Wong, M.L. Smith, Fibronectin fiber creep under constant force loading, Acta Biomater. 88 (2019) 78–85. https://doi.org/10.1016/J.ACTBIO.2019.02.022.

[40] R.F. Ker, Mechanics of tendon, from an engineering perspective, Int. J. Fatigue. 29 (2007) 1001–1009. https://doi.org/10.1016/j.ijfatigue.2006.09.020.

[41] F. Fang, S.P. Lake, Experimental evaluation of multiscale tendon mechanics; Experimental evaluation of multiscale tendon mechanics, J Orthop Res. 35 (2017) 1353–1365. https://doi.org/10.1002/jor.23488.

[42] E.M. Arruda, S. Calve, R.G. Dennis, K. Mundy, K. Baar, Regional variation of tibialis anterior tendon mechanics is lost following denervation, J Appl Physiol. 101 (2006) 1113–1117. https://doi.org/10.1152/japplphysiol.00612.2005.-De.

[43] SolarisTM Product Information | Smooth-On, Inc., (n.d.). https://www.smooth-on.com/products/solaris/ (accessed July 23, 2020).

[44] M.E. Wale, D.Q. Nesbitt, B.S. Henderson, C.K. Fitzpatrick, J.J. Creechley, T.J. Lujan, Applying ASTM Standards to Tensile Tests of Musculoskeletal Soft Tissue: Methods to Reduce Grip Failures and Promote Reproducibility, J. Biomech. Eng. 143 (2021). https://doi.org/10.1115/1.4048646.

[45] A. V. Sergueeva, J. Zhou, B.E. Meacham, D.J. Branagan, Gage length and sample size effect on measured properties during tensile testing, Mater. Sci. Eng. A. 526 (2009) 79–83. https://doi.org/10.1016/j.msea.2009.07.046.

[46] D. Eyrich, F. Brandl, B. Appel, H. Wiese, G. Maier, M. Wenzel, R. Staudenmaier, A. Goepferich, T. Blunk, Long-term stable fibrin gels for cartilage engineering, Biomaterials. 28 (2007) 55–65. https://doi.org/10.1016/j.biomaterials.2006.08.027.

[47] M. Okada, B. Blombäck, Calcium and fibrin gel structure, Thromb. Res. 29 (1983) 269–280. https://doi.org/10.1016/0049-3848(83)90039-7.

[48] S. Jordahl, L. Solorio, D.B. Neale, S. McDermott, J.H. Jordahl, A. Fox, C. Dunlay, A. Xiao, M. Brown, M. Wicha, G.D. Luker, J. Lahann, Engineered Fibrillar Fibronectin Networks as Three-Dimensional Tissue Scaffolds, Adv. Mater. 31 (2019). https://doi.org/10.1002/adma.201904580.

[49] A. Acuna, M.A. Drakopoulos, Y. Leng, C.J. Goergen, S. Calve, Three-dimensional visualization of extracellular matrix networks during murine development, Dev. Biol. 435 (2018) 122–129. https://doi.org/10.1016/J.YDBIO.2017.12.022.

[50] A. Acuna, S.H. Sofronici, C.J. Goergen, S. Calve, In Situ Measurement of Native Extracellular Matrix Strain, Exp. Mech. (2019) 1–15. https://doi.org/10.1007/s11340-019-00499-y.

[51] R.I. Litvinov, J.W. Weisel, Fibrin mechanical properties and their structural origins, Matrix Biol. 60–61 (2017) 110–123. https://doi.org/10.1016/j.matbio.2016.08.003.

[52] Admet, BioTense - Perfusion Bioreactor System, (n.d.). https://www.admet.com/wp-content/uploads/2015/07/ADMET-BioTense-Bioreactor-System-Brochure.pdf.

[53] K.L. Ruedinger, R. Medero, A. Rolda´n, R. Rolda´n-Alzate, Fabrication of Low-Cost Patient-Specific Vascular Models for Particle Image Velocimetry, Cardiovasc. Eng. Technol. 10 (n.d.). https://doi.org/10.1007/s13239-019-00417-2.

[54] M. Liu, J. Sun, Y. Sun, C. Bock, Q. Chen, Thickness-dependent mechanical properties of polydimethylsiloxane membranes, J. Micromechanics Microengineering. 19 (2009) 035028. https://doi.org/10.1088/0960-1317/19/3/035028.

[55] A. Shinde, S. Libring, A. Alpsoy, A. Abdullah, J.A. Schaber, L. Solorio, M.K. Wendt, Autocrine fibronectin inhibits breast cancer metastasis, Mol. Cancer Res. 16 (2018) 1579–1589. https://doi.org/10.1158/1541-7786.MCR-18-0151.

[56] K.A. Jansen, R.G. Bacabac, I.K. Piechocka, G.H. Koenderink, Cells actively stiffen fibrin networks by generating contractile stress, Biophys. J. 105 (2013) 2240–2251. https://doi.org/10.1016/j.bpj.2013.10.008.

[57] S. Britton, O. Kim, F. Pancaldi, Z. Xu, R.I. Litvinov, J.W. Weisel, M. Alber, Contribution of nascent cohesive fiber-fiber interactions to the non-linear elasticity of fibrin networks under tensile load, (2019). https://doi.org/10.1016/j.actbio.2019.05.068.

[58] L.K. Wood, E.M. Arruda, S. V. Brooks, Regional stiffening with aging in tibialis anterior tendons of mice occurs independent of changes in collagen fibril morphology, J. Appl. Physiol. 111 (2011) 999–1006. https://doi.org/10.1152/japplphysiol.00460.2011.

[59] P.M. Crapo, T.W. Gilbert, S.F. Badylak, An overview of tissue and whole organ decellularization processes, Biomaterials. 32 (2011) 3233–3243. https://doi.org/10.1016/j.biomaterials.2011.01.057.

[60] 3D Systems Solutions, Material Selection Guide for ProJet® MJP 2500 and 2500 Plus - VisiJet® M2 MultiJet Printing materials for functional precision plastic and elastomeric parts, (n.d.). https://www.3dsystems.com/sites/default/files/2020-08/3d-systems-visiJet-m2-material-selection-guide-usen-2020-08-20-web.pdf (accessed December 11, 2020).

REFERENCES

Abhilash, A. S., Baker, B. M., Trappmann, B., Chen, C. S., & Shenoy, V. B. (2014). Article Remodeling of Fibrous Extracellular Matrices by Contractile Cells: Predictions from Discrete Fiber Network Simulations. *Biophysj*, *107*, 1829–1840. https://doi.org/10.1016/j.bpj.2014.08.029

Ban, E., Wang, H., Matthew Franklin, J., Liphardt, J. T., Janmey, P. A., & Shenoy, V. B. (2019). Strong triaxial coupling and anomalous Poisson effect in collagen networks. *Proceedings of the National Academy of Sciences of the United States of America*, *116*(14), 6790–6799. https://doi.org/10.1073/pnas.1815659116

Bordeleau, F., Tang, L. N., & Reinhart-King, C. A. (2013). Topographical guidance of 3D tumor cell migration at an interface of collagen densities. *Physical Biology*, *10*(6), 736–740. https://doi.org/10.1088/1478-3975/10/6/065004

Breen, E. C. (2000). Mechanical strain increases type I collagen expression in pulmonary fibroblasts in vitro. *Journal of Applied Physiology*, *88*(1), 203–209. https://doi.org/10.1152/jappl.2000.88.1.203

Britton, S., Kim, O., Pancaldi, F., Xu, Z., Litvinov, R. I., Weisel, J. W., & Alber, M. (2019). *Contribution of nascent cohesive fiber-fiber interactions to the non-linear elasticity of fibrin networks under tensile load*. Acta Biomaterialia. https://doi.org/10.1016/j.actbio.2019.05.068

Brown, A. E. X., Litvinov, R. I., Discher, D. E., Purohit, P. K., & Weisel, J. W. (2009). Multiscale mechanics of fibrin polymer: Gel stretching with protein unfolding and loss of water. *Science*, *325*(5941), 741–744. https://doi.org/10.1126/science.1172484

Brown, A. E. X., Litvinov, R. I., Discher, D. E., & Weisel, J. W. (2007). Forced unfolding of coiled-coils in fibrinogen by single-molecule AFM. *Biophysical Journal*, *92*(5). https://doi.org/10.1529/biophysj.106.101261

Bruekers, S. M. C., Jaspers, M., Hendriks, J. M. A., Kurniawan, N. A., Koenderink, G. H., Kouwer, P. H. J., Rowan, A. E., & T. S. Huck, W. (2016). Fibrin-fiber architecture influences cell spreading and differentiation. In *Cell Adhesion and Migration* (Vol. 10, Issue 5, pp. 495–504). https://doi.org/10.1080/19336918.2016.1151607

Buganza Tepole, A., Gosain, A. K., & Kuhl, E. (2014). Computational modeling of skin: Using stress profiles as predictor for tissue necrosis in reconstructive surgery. *Computers and*

Structures, *143*, 32–39. https://doi.org/10.1016/j.compstruc.2014.07.004

Campbell, R. A., Aleman, M. M., Gray, L. D., Falvo, M. R., & Wolberg, A. S. (2010). Flow profoundly influences fibrin network structure: Implications for fibrin formation and clot stability in haemostasis. In *Thrombosis and Haemostasis* (Vol. 104, Issue 6, pp. 1281–1284). https://doi.org/10.1160/TH10-07-0442

Chandrashekar, A., Singh, G., Garry, J., Sikalas, N., & Labropoulos, N. (2018). Mechanical and Biochemical Role of Fibrin Within a Venous Thrombus. In *European Journal of Vascular and Endovascular Surgery* (Vol. 55, Issue 3, pp. 417–424). https://doi.org/10.1016/j.ejvs.2017.12.002

Collet, J. P., Park, D., Lesty, C., Soria, J., Soria, C., Montalescot, G., & Weisel, J. W. (2000). Influence of fibrin network conformation and fibrin diameter on fibrinolysis speed: Dynamic and structural approaches by confocal microscopy. *Arteriosclerosis, Thrombosis, and Vascular Biology*, *20*(5), 1354–1361. https://doi.org/10.1161/01.ATV.20.5.1354

Doube, M., Klosowski, M. M., Arganda-Carreras, I., Cordelières, F. P., Dougherty, R. P., Jackson, J. S., Schmid, B., Hutchinson, J. R., & Shefelbine, S. J. (2010). BoneJ: Free and extensible bone image analysis in ImageJ. *Bone*, *47*(6), 1076–1079. https://doi.org/10.1016/j.bone.2010.08.023

Duan, C., Jimenez, J. M., Goergen, C., Cox, A., Sivasankar, P. M., & Calve, S. (2021). Hydration State and Hyaluronidase Treatment Significantly Affect Porcine Vocal Fold Biomechanics. *Journal of Voice*. https://doi.org/10.1016/j.jvoice.2021.01.014

Elhebeary, M., Emon, M. A. B., Aydin, O., & Saif, M. T. A. (2019). A novel technique for in situ uniaxial tests of self-assembled soft biomaterials. *Lab on a Chip*, *19*(7), 1153–1161. https://doi.org/10.1039/c8lc01273c

Emon, B., Li, Z., Joy, M. S. H., Doha, U., Kosari, F., & Saif, M. A. T. (2021). A novel method for sensor-based quantification of single/multicellular force dynamics and stiffening in 3D matrices. *Science Advances*, *7*(15), eabf2629. https://doi.org/10.1126/SCIADV.ABF2629

Enríquez, Á., Libring, S., Field, T. C., Jimenez, J., Lee, T., Park, H., Satoski, D., Wendt, M. K., Calve, S., Tepole, A. B., Solorio, L., & Lee, H. (2021). High-Throughput Magnetic Actuation Platform for Evaluating the Effect of Mechanical Force on 3D Tumor Microenvironment. *Advanced Functional Materials*, *31*(1), 1–12. https://doi.org/10.1002/adfm.202005021

Fish, R. J., & Neerman-Arbez, M. (2012). Fibrinogen gene regulation. *Thrombosis and*

Haemostasis, *108*(3), 419–426. https://doi.org/10.1160/TH12-04-0273

Frith, J. E., Kusuma, G. D., Carthew, J., Li, F., Cloonan, N., Gomez, G. A., & Cooper-White, J. J. (2018). Mechanically-sensitive miRNAs bias human mesenchymal stem cell fate via mTOR signaling. *Nature Communications*, *9*(1). https://doi.org/10.1038/s41467-017-02486-0

Gasser, T. C., Ogden, R. W., & Holzapfel, G. A. (2006). Hyperelastic modelling of arterial layers with distributed collagen fibre orientations. *Journal of the Royal Society Interface*, *3*(6), 15–35. https://doi.org/10.1098/rsif.2005.0073

Gilchrist, C. L., Ruch, D. S., Little, D., & Guilak, F. (2014). *Micro-scale and meso-scale architectural cues cooperate and compete to direct aligned tissue formation*. https://doi.org/10.1016/j.biomaterials.2014.08.047

Janmey, P. A., Winer, J. P., & Weisel, J. W. (2009). Fibrin gels and their clinical and bioengineering applications. In *Journal of the Royal Society Interface* (Vol. 6, Issue 30, pp. 1–10). Royal Society. https://doi.org/10.1098/rsif.2008.0327

Kessler, D., Dethlefsen, S., Haase, I., Plomann, M., Hirche, F., Krieg, T., & Eckes, B. (2001). Fibroblasts in Mechanically Stressed Collagen Lattices Assume a "Synthetic" Phenotype*. *Journal of Biological Chemistry*, *276*, 36575–36585. https://doi.org/10.1074/jbc.M101602200

Lai, V. K., Frey, C. R., Kerandi, A. M., Lake, S. P., Tranquillo, R. T., & Barocas, V. H. (2012). Microstructural and mechanical differences between digested collagen-fibrin co-gels and pure collagen and fibrin gels. *Acta Biomaterialia*, *8*(11), 4031–4042. https://doi.org/10.1016/j.actbio.2012.07.010

Leng, Y., Calve, S., & Tepole, A. B. (2021). *Predicting the Mechanical Properties of Fibrin Using Neural Networks Trained on Discrete Fiber Network Data*. 1–20. http://arxiv.org/abs/2101.11712

Li, W., Sigley, J., Baker, S. R., Helms, C. C., Kinney, M. T., Pieters, M., Brubaker, P. H., Cubcciotti, R., & Guthold, M. (2017). *Nonuniform Internal Structure of Fibrin Fibers: Protein Density and Bond Density Strongly Decrease with Increasing Diameter*. https://doi.org/10.1155/2017/6385628

Lindahl, G. E., Chambers, R. C., Papakrivopoulou, J., Dawson, S. J., Jacobsen, M. C., Bishop, J. E., & Laurent, G. J. (2002). Activation of fibroblast procollagen α1(I) transcription by mechanical strain is transforming growth factor-β-dependent and involves increased binding

of CCAAT-binding factor (CBF/NF-Y) at the proximal promoter. *Journal of Biological Chemistry*, *277*(8), 6153–6161. https://doi.org/10.1074/jbc.M108966200

Lloyd, A. A., Wang, Z. X., & Donnelly, E. (2015). Multiscale Contribution of Bone Tissue Material Property Heterogeneity to Trabecular Bone Mechanical Behavior. *Journal of Biomechanical Engineering*, *137*(1). https://doi.org/10.1115/1.4029046

Magatti, D., Molteni, M., Cardinali, B., Rocco, M., & Ferri, F. (2013). Modeling of fibrin gels based on confocal microscopy and light-scattering data. *Biophysical Journal*, *104*(5), 1151–1159. https://doi.org/10.1016/j.bpj.2013.01.024

Miron-Mendoza, M., Graham, E., Manohar, S., & Petroll, W. M. (2017). Fibroblast-fibronectin patterning and network formation in 3D fibrin matrices. *Matrix Biology*, *64*, 69–80. https://doi.org/10.1016/j.matbio.2017.06.001

Molteni, M., Magatti, D., Cardinali, B., Rocco, M., & Ferri, F. (2013). Fast two-dimensional bubble analysis of biopolymer filamentous networks pore size from confocal microscopy thin data stacks. *Biophysical Journal*, *104*(5), 1160–1169. https://doi.org/10.1016/j.bpj.2013.01.016

Moutos, F. T., & Guilak, F. (2008). Composite scaffolds for cartilage tissue engineering. *Biorheology*, *45*(3–4), 501–512. https://doi.org/10.1088/1478-3975/10/6/065004

Münster, S., Jawerth, L. M., Leslie, B. A., Weitz, J. I., Fabry, B., & Weitz, D. A. (2013). Strain history dependence of the nonlinear stress response of fibrin and collagen networks. *Proceedings of the National Academy of Sciences of the United States of America*, *110*(30), 12197–12202. https://doi.org/10.1073/pnas.1222787110

Neeves, K. B., Illing, D. A. R., & Diamond, S. L. (2010). Thrombin flux and wall shear rate regulate fibrin fiber deposition state during polymerization under flow. *Biophysical Journal*, *98*(7), 1344–1352. https://doi.org/10.1016/j.bpj.2009.12.4275

Nikolova, M. P., & Chavali, M. S. (2019). Recent advances in biomaterials for 3D scaffolds: A review. *Bioactive Materials*, *4*, 271–292. https://doi.org/10.1016/j.bioactmat.2019.10.005

Pathare, S. J., Eng, W., Lee, S.-J. J., & Ramasubramanian, A. K. (2021). Fibrin Prestress Due to Platelet Aggregation and Contraction Increases Clot Stiffness. *BioRxiv*, 4400330. https://doi.org/https://doi.org/10.1101/2021.04.19.440330

Piechocka, I. K., Bacabac, R. G., Potters, M., Mackintosh, F. C., & Koenderink, G. H. (2010). Structural hierarchy governs fibrin gel mechanics. *Biophysical Journal*, *98*(10), 2281–2289.

https://doi.org/10.1016/j.bpj.2010.01.040

Podhorská, B., Vetrík, M., Chylíková-Krumbholcová, E., Kománková, L., Banafshehvaragh, N. R., Šlouf, M., Dušková-Smrčková, M., & Janoušková, O. (2020). Revealing the true morphological structure of macroporous soft hydrogels for tissue engineering. *Applied Sciences (Switzerland)*, *10*(19). https://doi.org/10.3390/APP10196672

Püspöki, Z., Storath, M., Sage, D., & Unser, M. (2016). Transforms and operators for directional bioimage analysis: A survey. *Advances in Anatomy Embryology and Cell Biology*, *219*, 69–93. https://doi.org/10.1007/978-3-319-28549-8_3

Rezakhaniha, R., Agianniotis, · A, Schrauwen, · J T C, Griffa, · A, Sage, · D, Bouten, · C V C, Van De Vosse, · F N, Unser, · M, Stergiopulos, · N, Schrauwen, J. T. C., Griffa, A., Sage, D., Bouten, C. V. C., & Agianniotis, A. (2012). Experimental investigation of collagen waviness and orientation in the arterial adventitia using confocal laser scanning microscopy. *Biomech Model Mechanobiol*, *11*, 461–473. https://doi.org/10.1007/s10237-011-0325-z

Ryan, E. A., Mockros, L. F., Weisel, J. W., & Lorand, L. (1999). Structural origins of fibrin clot rheology. *Biophysical Journal*, *77*(5), 2813–2826. https://doi.org/10.1016/S0006-3495(99)77113-4

Sander, E. A., Barocas, V. H., & Tranquillo, R. T. (2011). Initial fiber alignment pattern alters extracellular matrix synthesis in fibroblast-populated fibrin gel cruciforms and correlates with predicted tension. *Annals of Biomedical Engineering*, *39*(2), 714–729. https://doi.org/10.1007/s10439-010-0192-2

Schultz, G. S., Ladwig, G., & Wysocki, A. (2005). Extracellular matrix: Review of its roles in acute and chronic wounds. In *World Wide Wounds* (Vol. 2005). http://www.worldwidewounds.com/2005/august/Schultz/Extrace-Matric-Acute-Chronic-Wounds.html

Silvain, J., Collet, J. P., Nagaswami, C., Beygui, F., Edmondson, K. E., Bellemain-Appaix, A., Cayla, G., Pena, A., Brugier, D., Barthelemy, O., Montalescot, G., & Weisel, J. W. (2011). Composition of coronary thrombus in acute myocardial infarction. *Journal of the American College of Cardiology*, *57*(12), 1359–1367. https://doi.org/10.1016/j.jacc.2010.09.077

Sugerman, G. P., Parekh, S. H., & Rausch, M. K. (2020). Nonlinear, dissipative phenomena in whole blood clot mechanics. *Cite This: Soft Matter*, *16*, 9908. https://doi.org/10.1039/d0sm01317j

Tepole, A. B. (2017). Computational systems mechanobiology of wound healing. *Comput. Methods Appl. Mech. Engrg.*, *314*, 46–70. https://doi.org/10.1016/j.cma.2016.04.034

Tonti, O. R., Larson, H., Lipp, S. N., Luetkemeyer, C. M., Makam, M., Vargas, D., Wilcox, S. M., & Calve, S. (2021). Tissue-specific parameters for the design of ECM-mimetic biomaterials. In *Acta Biomaterialia*. https://doi.org/10.1016/j.actbio.2021.04.017

Urbanczyk, M., Layland, S. L., & Schenke-Layland, K. (2020). *The role of extracellular matrix in biomechanics and its impact on bioengineering of cells and 3D tissues*. Matrix Biology. https://doi.org/10.1016/j.matbio.2019.11.005

Wang, Y., Kumar, S., Nisar, A., Bonn, M., Rausch, M. K., & Parekh, S. H. (2021). Probing fibrin's molecular response to shear and tensile deformation with coherent Raman microscopy. *Acta Biomaterialia*, *121*, 383–392. https://doi.org/10.1016/j.actbio.2020.12.020

Weisel, J. W. (2004). *The mechanical properties of fibrin for basic scientists and clinicians*. *112*, 267–276. https://doi.org/10.1016/j.bpc.2004.07.029

Weisel, J. W., & Litvinov, R. I. (2013). Mechanisms of fibrin polymerization and clinical implications. *The American Society of Hematology*, *121*(10), 1712–1719. https://doi.org/10.1182/blood-2012-09-306639.

Weisel, J. W., & Litvinov, R. I. (2017). Fibrin formation, structure and properties. *Sub-Cellular Biochemistry*, *82*, 405–456. https://doi.org/10.1007/978-3-319-49674-0_13

Xia, J., Cai, L. H., Wu, H., MacKintosh, F. C., & Weitz, D. A. (2021). Anomalous mechanics of Zn2+-modified fibrin networks. *Proceedings of the National Academy of Sciences of the United States of America*, *118*(10). https://doi.org/10.1073/pnas.2020541118

Yesudasan, S., & Averett, R. D. (2020). Multiscale network modeling of fibrin fibers and fibrin clots with protofibril binding mechanics. *Polymers*, *12*(6). https://doi.org/10.3390/POLYM12061223

Zhmurov, A., Protopopova, A. D., Litvinov, R. I., Zhukov, P., Mukhitov, A. R., Weisel, J. W., & Barsegov, V. (2016). Structural Basis of Interfacial Flexibility in Fibrin Oligomers. *Structure*, *24*(11), 1907–1917. https://doi.org/10.1016/j.str.2016.08.009